Shape from Shading: a well-posed problem?

Emmanuel Prados, Olivier Faugeras, Fabio Camilli

INSTITUT NATIONAL DE RECHERCHE EN INFORMATIQUE ET EN AUTOMATIQUE

Shape from Shading: a well-posed problem?

Emmanuel Prados — Olivier Faugeras — Fabio Camilli

N° 5297

August 2004

Thème COG

ISSN 0249-6399 ISRN INRIA/RR--5297--FR+ENG

INRIA
SOPHIA ANTIPOLIS

Shape from Shading: a well-posed problem?

Emmanuel Prados* , Olivier Faugeras† , Fabio Camilli‡

Thème COG — Systèmes cognitifs
Projet Odyssée

Rapport de recherche n° 5297 — August 2004 — 55 pages

Abstract: Shape From Shading is known to be an ill-posed problem. Contrary to the previous work, we show here that if *we model the problem in a more realistic way than it is usually done* (we take into account the $1/r^2$ attenuation term of the lighting), Shape From Shading can be *completely well-posed*. Thus the shading allows to recover (almost) any surface from only one image (of this surface), without any additional data (in particular, without regularity assumptions and without the knowledge of the heights of the solution at the local "minima", contrary to [16, 52]). More precisely, in this report we formulate the problem as that of solving a *new PDE*, we develop a *complete mathematical study* of this equation (existence and uniqueness of the solution) and we design a new *provably convergent numerical method*. Finally, we test our new SFS method on various synthetic images and on our database of *real images* of faces, with success.

Key-words: Shape From Shading, $1/r^2$ lighting attenuation term, real image database, well-posed problem, viscosity solutions, provably convergent algorithms.

* http://www-sop.inria.fr/odyssee/ (Odyssée Lab.,INRIA/ENS/ENPC,France)
† http://www-sop.inria.fr/odyssee/ (Odyssée Lab.,INRIA/ENS/ENPC,France)
‡ camilli@ing.univaq.it (Pure and Applied Mathematics Dept. of the University of L'Aquila, Italy)

Unité de recherche INRIA Sophia Antipolis
2004, route des Lucioles, BP 93, 06902 Sophia Antipolis Cedex (France)
Téléphone : +33 4 92 38 77 77 —Télécopie : +33 4 92 38 77 65

"Shape-from-Shading": un problème bien posé ?

Résumé : Le "Shape From Shading" est connu pour être un problème mal posé. Contrairement aux précédents travaux, nous montrons ici que si le problème est modélisé de manière plus réaliste (nous prenons en compte le terme d'atténuation en $1/r^2$ de l'éclairage), le problème du "Shape From Shading" peut devenir complètement bien posé. Plus précisément, dans ce rapport nous formulons le problème sous la forme d'une nouvelle équation aux dérivées partielles, nous développons une étude mathématique complète de cette équation (existence et unicité de la solution), et nous proposons une nouvelle méthode numérique dont nous prouvons la convergence. Enfin, nous testons avec succès notre méthode sur diverses images synthétiques et sur notre base de données d'images réelles.

Mots-clés : "Shape From Shading", atténuation de l'éclairage, base de données d'images réelles, problème bien posé, solutions de viscosité.

1 Introduction and related work

Shape from shading (SFS) has been a central problem in the field of computer vision from the early days on. The problem is to compute the three-dimensional shape of a surface from the brightness variations in a black and white image of that surface. It is well known that this problem is ill-posed. In particular a number of articles show that the solution is not unique [7, 45, 40, 56, 5, 18, 53, 49]. This problem has often been illustrated by such

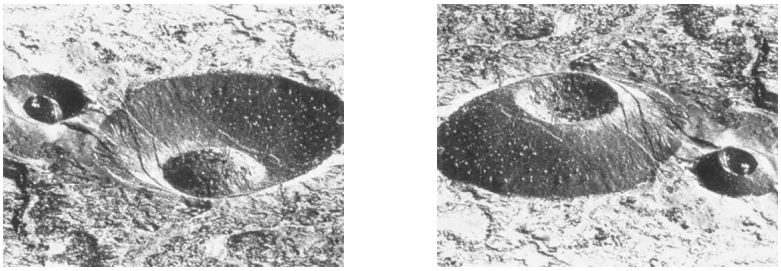

a) b)

Figure 1: The crater illusion [45]. From picture a), we perceive two craters, a small and a big one. But we can turn these craters into volcanoes (although upside down) if we imagine the light source to be at the bottom of the picture rather than at the top. This picture is actually that of a pair of ash cones in the Hawaiian Island, not that of a pair of craters; figure b) displays the picture correctly.

concave/convex ambiguities as the one displayed in Figure 1. In this figure, the ambiguity is due to a change of the estimation of the parameters of the lighting. In fact, this kind of ambiguity can be widely generalized. In effect, in [5], Belhumeur and colleagues prove that when the lighting direction[1] and the Lambertian reflectance (albedo) of the surface are unknown, then the same image can be obtained by a continuous family of surfaces (depending linearly of three parameters). In other words, they show that neither shading nor shadowing of an objet, seen from a single viewpoint reveals its exact 3D structure. This is the "Bas-relief Ambiguity", see [5] and Figure 2. Being aware of these difficulties, we therefore assume in this paper that all the parameters of the light

a) b)

Figure 2: "Bas-relief Ambiguity" [5]: Frontal and side views of a marble bas-relief sculpture. Notice how the frontal views appear to have full 3-dimensional depth, while the side view reveals the flattening. This demonstrates that the image a) can be produced by two surfaces: the three-dimensional surface we imagine by visualizing image a) and the actual bas-relief which is at the origin of the two photos a) and b). For more details, the reader can refer to [5].

source, the surface reflectance and the camera are known. Nevertheless this knowledge is not sufficient to get rid of some concave/convex ambiguities. In effect, even though they assume complete control of the experimental setup, Dupuis and Oliensis, Rouy and Tourin, Durou and Piau or Prados and Faugeras [40, 56, 18, 53, 49] are hampered by this kind of difficulty. For example, let us focus on the "Eikonal" framework used in [56, 35]. Rouy and colleagues assume that the camera performs an orthographic projection of the scene, that the surface is Lambertian and that the light source direction[2] is the same as that of the axis of the camera. In this setup, a concave/convex duality clearly appears, see Figures 3 and 4. The surfaces represented in Figure 3-a) and in

[1] In the case of a distant light source.
[2] We consider here that the light source is at infinity.

Figure 3-b) yield the same image. This also holds for the more complex surfaces represented in Figures 4-a),4-b), 4-c) and 4-d). In these figures, the various surfaces have been obtained from the surfaces a) by applying horizontal symmetries. Today, this concave/convex ambiguity is well understood. It is due to the existence

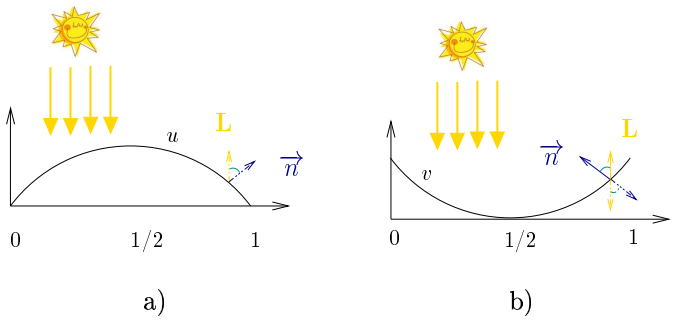

Figure 3: Concave/convex duality in the Eikonal framework: The surfaces a) and b) yield the same image.

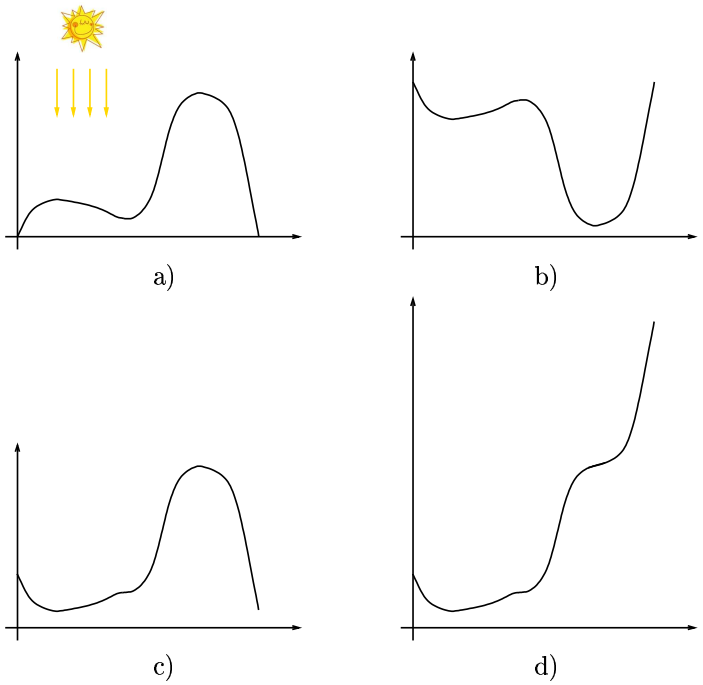

Figure 4: Consequences of the concave/convex duality in the Eikonal framework. Examples of more complex surfaces. The surfaces a), b), c) and d) yield the same image...

of singular points[3], see [56]. The presence of the singular points is due to the modeling. In particular it is due to the fact that the authors assume that the scene is illuminated by a single point light source located at infinity (or to the fact that they neglect the $1/r^2$ attenuation term in the brigthness equation, see section 2). Also, this kind of ambiguity holds for the orthographic SFS [56, 53] as well as for the perspective SFS [49, 50] problem. In particular, it holds even when the light source direction does not coincide with the camera axis. For a complete and generic study, the reader can refer to [51, 48]... Nevertheless, *in contradiction with all these results, we prove in this paper that the Shape from Shading problem can be well-posed.* Not surprisingly, this result is obtained by considering a more realistic image formation model.

These last ten years, various authors have attempted to improve the applicability of the Shape from shading methods by modeling the physics of the problem, in particular the illumination process, in a more realistic manner. In a similar vein, Bakshi, or Lee and Kuo [1, 33] propose a solution for some non-Lambertian Shape from Shading problems. Some authors take into account the interreflections [59, 21]. Other authors deal with

[3] The singular points are the pixels of the image corresponding to points of the surface such that the surface normal coincides with the light direction. These points have maximal brightness. They are also called "critical points".

multiple light sources [62]. Finally, various solutions have been proposed for taking into account the perspective effect [44, 32, 22, 64, 65, 49, 61, 11, 12]. Looking at some recent Shape from Shading surveys[4], one may have the feeling that the work of [1, 33, 59, 21, 62, 44, 32, 22, 64, 65, 49, 61, 11, 12] has appeared too early, insofar as the existing Shape from Shading methods dealing with the traditional framework, i.e. Lambertian surface + light source at infinity + orthographic projection, are quite unsatisfactory[5] even with very simple synthetic images verifying the modeling hypotheses. Also, since we are not able to solve the simplest version of the SFS problem, it seems unreasonable to attempt to solve this problem by modeling it in a more complex way. *In this paper, we hope to remove this feeling.*

One of the reasons why SFS is ill-posed is the over-simplification in the modeling. In this paper, we prove that by using more realistic hypotheses than the classical ones, the Shape from Shading becomes well-posed (modulo some weak a priori on the creases of the solution near the boundary). As a consequence it becomes easier to solve. In detail, we assume that the camera is a pinhole and that the light source is located at the optical center. Nevertheless, contrary to [50], we do not neglect the $1/r^2$ attenuation term (see section 2). As proved in section 4, this "new" term makes the problem better posed. In particular, the notion of singular points does not make sense anymore and the concave/convex duality disappears.

This article first describes a *complete theoretical study* of the Shape from Shading problem in this particular setup (section 4). Second, it proposes an *original and rigorous numerical method* allowing to approximate numerically the solutions of the problem. We detail a stable and consistent approximation scheme and we describe a provably convergent numerical algorithm (section 5). Finally, we demonstrate the practical relevance of our method by displaying some experimental results (section 6).

2 Modeling of the SFS problem

In this section, we recall the image formation process. To do this, we will upstream the light ray from the optical system to the light source. For more details we refer to [25].

- We start with the relationship between the image brightness and the surface radiance. This relationship is well-known, see for example [25]:

$$E_i = L_s \frac{\pi}{4} \left(\frac{d}{f}\right)^2 \cos^4 \alpha \ , \tag{1}$$

  where E_i is image irradiance, which is assumeed to be equal to the image brightness. L_s denotes the surface radiance[6]. d is the diameter of the lens, f is the focal length and α is the angle between optical axis and the line of sight to a surface point of a corresponding image point. Because the term $\cos^4 \alpha$ is easily derived from the image coordinates and can be compensated for, image brightness is substantially proportional to surface irradiance.

- Next we assume that the scene is illuminated by a single point light source and that there are not inter-reflections. In this case, the relationship between the radiance L_s of a point of the surface (in the view direction) with the surface normal (at this point) and the light source direction is generally described by the Bi-directional Reflectance Distribution Function (BRDF):

$$L_s = F(\theta_i, \theta_r, \phi_r) E_s \ , \tag{2}$$

  where E_s is the irradiance of the surface and the angles θ_i, θ_r and ϕ_r are described in Figure 5. In this figure N is the object surface normal, L is the direction to the light source, and V is the direction to the viewer. θ_i is the angle between L and N, and θ_r is the angle between V and N, respectively. ϕ_r is the azimuthal angle between L and V with respect to the surface normal N.
  A fundamental example: An ideal *Lambertian* surface is one that appears equally bright from all viewing directions and reflects all incident light, absorbing none. Its BRDF is then a constant ($\frac{1}{\pi}$, see [25]) and we have:

$$L_s = \frac{1}{\pi} E_s. \tag{3}$$

[4] For example [66, 17].
[5] See the results shown in [66, 17].
[6] i.e. the radiance of the surface in the direction of the viewer (the optical center).

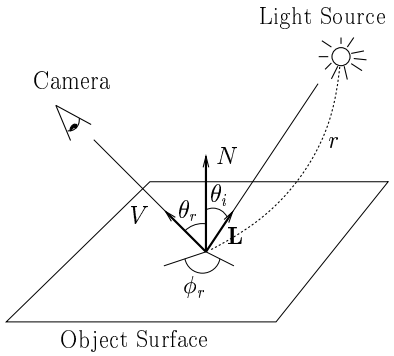

Figure 5: The surface local coordinate system (see [37, 25]).

- Finally, we describe the irradiance E_s of the surface point. We have (see [25]):

$$E_s = I_0 \ \frac{\cos\theta_i}{r^2} \tag{4}$$

where I_0 is the intensity of the light source and r is the distance between the light source and the considered surface point.

In summary, combining (1),(2) and (4), the brightness image is given by:

$$E_i = \sigma_1 \ F(\theta_i, \theta_r, \phi_r) \ \frac{\cos\theta_i}{r^2} \ , \tag{5}$$

where σ_1 is a constant coefficient related to the parameters of imaging system and the intensity of the light source.
For a Lambertian surface, the brightness image is then:

$$E_i = \sigma_2 \ \frac{\cos\theta_i}{r^2}, \tag{6}$$

σ_2 being a constant coefficient.

Remarks:

1. In the case where the light source is located far from the surface[7], the variations of the brightness of the image is essentially due to those of $\cos\theta_i$ and we can assume that r is constant. In this case the brightness image is given by:
$$E_i = \sigma_3 \ F(\theta_i, \theta_r, \phi_r) \ \cos\theta_i, \tag{7}$$
where σ_3 is a constant coefficient. For a Lambertian surface, the brightness image is even simpler:
$$E_i = \sigma_4 \ \cos\theta_i \tag{8}$$
(σ_4 being a constant coefficient).
2. In the particular case where the viewer direction coincides with the light source direction, equation (5) can be rewritten as:
$$E_i = \sigma_1 \ \frac{G(\cos\theta_i)}{r^2}, \tag{9}$$
where $G(t) = F(arccos(t), arccos(t), 0) \ t$.

In the Shape from Shading literature, the surface is always assumed Lambertian (except, to our knowledge, for very few papers [1, 36, 33]) and the light source is unique, reduced to a point and located at infinity (except for an extremely small number of papers [36, 63, 10]). To simplify even more the problem, the authors usually assume that the camera performs an orthographic projection of the scene. Recently, in order to increase the

[7] i.e. the normal vector $N(x)$ (or $\cos\theta_i(x)$) "varies more than" the distance $r(x)$, when the point x parameterizes the surface.

applicability of the Shape from Shading, various SFS methods have been extended to pinhole (perspective) cameras [44, 32, 22, 36, 64, 65, 49, 61, 11, 12].

As Okatani and Deguchi [36] and Prados and Faugeras [50] we model the camera as a *pinhole* (therefore we assume that the camera performs a perspective projection of the scene) and we assume that the scene is illuminated by a single point light source *located at the optical center* (hence not at infinity). Note that, beside the theoretical interest of our approach, this modeling is quite relevant for many applications. In effect, it nicely corresponds to the situation encountered in some medical protocols like endoscopy in which the (point) light source is located very close to the camera, because of space constraints, see [37, 50] for an application of SFS in this area. This modeling also corresponds approximately to the situation encountered when we use a simple camera equiped with a flash; see [50] for two applications (face reconstruction and page restoration).

3 Mathematical formulation of the SFS problem

In this section, we formulate the SFS problem as that of solving a Partial Differential Equation (PDE). We describe some Hamilton-Jacobi equations arising from equation (6) and we detail the associated Hamiltonians. Let Ω be an open subset of $\mathbb{R}^2$. Ω represents the image domain, e.g., the rectangle $]0, X[\times]0, Y[$. We represent the scene by a surface $\mathcal{S}$ which can be explicitly parameterized by using the function $S : \overline{\Omega} \to \mathbb{R}^3$:

$$\mathcal{S} = \left\{ S(x); \quad x \in \overline{\Omega} \right\},$$

where

$$S(x) = \frac{f\ u(x)}{\sqrt{|x|^2 + f^2}}\ (x, -f).$$

$f > 0$ denotes the focal length, see Figure 6.

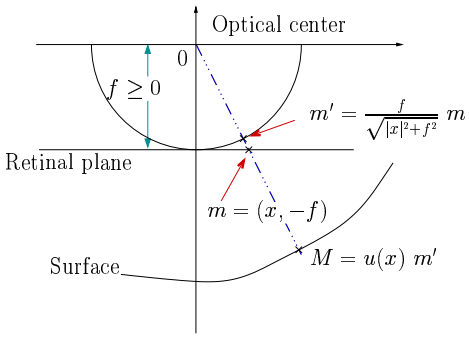

Figure 6: The brightness of the "pixel" $(x, -f)$ is associated to the irradiance of the point $u(x)\frac{f}{\sqrt{|x|^2+f^2}}(x, -f)$ on the surface $\mathcal{S}$.

For such a surface $\mathcal{S}$, a normal vector $\mathbf{n}(x)$ at the point $S(x)$ is given by[8]:

$$\mathbf{n}(x) = \left(f\nabla u(x) - \frac{fu(x)}{|x|^2 + f^2}\ x\ ,\ \nabla u(x) \cdot x + \frac{fu(x)}{|x|^2 + f^2}\ f \right).$$

Note: It is possible to parameterize differently the surface $\mathcal{S}$; for example, we can define

$$S(x) = u(x)(x, -f), \qquad \forall x \in \overline{\Omega}.$$

In this case, we have

$$\mathbf{n}(x) = \left(f\nabla u(x)\ ,\ u(x) + x \cdot \nabla u(x) \right).$$

For $y \in \mathbb{R}^3$, we denote $\mathbf{L}(y)$ the unit vector representing the light source direction at the point y. Since we assume that the light source is located at the optical center, the vector $\mathbf{L}(S(x))$ is equal to[9]:

$$\mathbf{L}(S(x)) = 1/\sqrt{|x|^2 + f^2}\ (-x, f).$$

[8] The two columns of the Jacobian $DS(x)$ are tangent vectors to $\mathcal{S}$ at the point $S(x)$. Their cross-product is a normal vector.
[9] We choose $\mathbf{L}(S(x))$ such that its third coordinate is positive.

Now, let us assume that the surface is *Lambertian*. If we denote $I(x) = \frac{E_i(x)}{\sigma_2}$, the brightness equation (6) becomes[10]:

$$I(x) = \frac{\cos\theta_i}{r^2}. \tag{10}$$

Since $\cos\theta_i$ is the dot product

$$\cos\theta_i = \mathbf{L}(S(x)) \cdot \frac{\mathbf{n}(x)}{|\mathbf{n}(x)|}$$

and

$$r = fu(x),$$

we obtain from (10) the following PDE:

$$I(x) = \frac{u(x)}{\sqrt{[f^2|\nabla u(x)|^2 + (\nabla u(x)\cdot x)^2]/Q(x)^2 + u(x)^2}} \frac{1}{f^2 u(x)^2}, \tag{11}$$

where $Q(x) = \sqrt{f^2/(|x|^2+f^2)}$. For convenience we rewrite Equation (11) as:

$$I(x) f^2 \frac{\sqrt{[f^2|\nabla u(x)|^2 + (\nabla u(x)\cdot x)^2]/Q(x)^2 + u(x)^2}}{u(x)} - u(x)^{-2} = 0. \tag{12}$$

If we assume that the surface $\mathcal{S}$ is visible, i.e. in front of the optical center, u is strictly positive, see Figure 6. This allows us to simplify equation (12) by using the *change of variables* $v = ln(u)$:

$$-e^{-2v(x)} + J(x)\sqrt{f^2|\nabla v(x)|^2 + (\nabla v(x)\cdot x)^2 + Q(x)^2} = 0, \tag{13}$$

where $J(x) = \frac{I(x)f^2}{Q(x)}$ is a positive function. To this equation, we associate the *Hamiltonian*

$$H_F(x,u,p) = -e^{-2u} + J(x)\sqrt{f^2|p|^2 + (p\cdot x)^2 + Q(x)^2}.$$

Note: In the case where we parameterize $\mathcal{S}$ by $S(x) = u(x)(x,-f)$, we obtain the equation

$$-e^{-2v(x)} + J(x)\sqrt{f^2|\nabla v(x)|^2 + (\nabla v(x)\cdot x + 1)^2} = 0, \tag{14}$$

instead of (13), and the Hamiltonian

$$H'_F(x,u,p) = -e^{-2u} + J(x)\sqrt{f^2|p|^2 + (p\cdot x + 1)^2}$$

instead of H_F. All the results presented in this paper can be obtained with either equation (13) or (14) and the associated Hamiltonians. Since the Hamiltonian H_F is mathematically simpler than H'_F [11] therefore in the sequel, we work only with the first one and its associated equation.

In [36, 37], Okatani and Deguchi do not formalize the problem with PDEs (in particular equation (13)), and the associated Hamiltonians H_F. Let us emphasize that stating the problem as that of solving PDEs is a fundamental preliminary step for a theoretical study, for example for proving the uniqueness of the solution.

4 Shape from Shading can be a completely well-posed problem!

4.1 Related work

To our knowledge, only Okatani and Deguchi [36], and Prados and Faugeras [50] deal with the model considered here (pinhole camera and light source at the optical center).

[10] We assume that all the parameters of the camera (diameter of lens, focal length...), of the light source and of the surface (albedo) are known. Therefore σ_2 and hence $I(x)$ are known.

[11] For example, For some fixed (x,u), $H_F(x,u,p)$ reaches its minimum at $p=0$. Also, the application $\lambda \mapsto H_F(x,u,\lambda p)$ is nondecreasing for $\lambda \in \mathbb{R}^+$. These properties do not hold for the Hamiltonian H'_F.

In [36], Okatani and Deguchi do not address at all the theoretical question of existence and uniqueness of a solution. Also, they do not write the adequate Hamilton-Jacobi equation (as we do in section 3). They only propose a numerical method based on the propagation of the iso-distance contours, turning the static equation (5) into an evolution equation.

In [50], Prados and Faugeras deal with equation (8) but not with equation (6). They neglect the $1/r^2$ term. By simplifying the modeling, they think they simplify the problem. On the contrary, they make it more complex. In effect, as explained in [51, 48] by ignoring the $1/r^2$ attenuation term the problem becomes ill-posed: the uniqueness of the solution does not hold. To obtain a unique solution one needs to specify Dirichlet boundary conditions on the boundary of the image and *at all the singular points* [51, 48] (as in the case of a distant point light source [56, 53, 49]).

To get around this difficulty[12] Prados and colleagues [52, 47, 50] obtain the uniqueness of a maximal solution by using sophisticated mathematical tools. Even if they obtain excellent numerical results with real images with a unique singular point [50, 47], their method presents some difficulties when there exist several singular points. Aware of the major role played by the singular points, Oliensis and Dupuis [41] and Kimmel and Bruckstein [29] propose some "global" methods (based on the nature of these particular points) allowing to recover some (very) smooth and constrained surfaces[13] (in the case where these surfaces exist). Okatani and Deguchi, in [38, 39], use the isophotes of the image for classifying part of the singular points. They also suggest how to use the informations they obtain for improving the global methods of Dupuis and Oliensis [41] and of Kimmel and Bruckstein [29].

Note that although the papers [41, 29, 38, 39] are based on an orthographic camera and a single distant light source, this work can be easily extended to the more realistic modeling of [50] by using the tools developed in [47, 52]. Nevertheless, despite their advantages, these global methods [41, 29, 38, 39] have an important weakness. In effect, in practice, because of noise, of errors on the parameters (focal length, light position, etc...) and of incorrect modeling (interrecflections, spatially extended light source, non-lambertian reflectance...) the SFS equations (such as those described in [41, 29, 50]) do not have smooth solutions! Also, the global methods proposed in [41, 29, 38] are quite disappointing when applied to real images. These global methods tend to return satisfying results only with simple synthetic images.
Opposite to all the previous work [56, 53, 49, 52, 47, 50, 41, 29, 38, 39], let us stress that *the notion of singular points does not make any sense as soon as we do not neglect the* $1/r^2$ *attenuation term.* This is particularly relevant in the framework considered in this paper, i.e. a pinhole camera with a single light source located at the optical center. As a result of a more realistic modeling, the difficulties described above completely disappear.

The results presented in the next section are based on the notion of viscosity solutions of the Hamilton-Jacobi PDEs. Let us recall that the viscosity solutions are solutions in a weak sense and that the classical (differentiable) solutions are particular viscosity solutions. The notion of viscosity solutions has been introduced by Crandall and Lions [34, 14, 13]. For more recent results, we refer the reader to [2, 3]. For an intuitive approach connected to computer vision, see [48]. The reader can also browse through the first sections of [54].

4.2 Well-posedness of the SFS problem

Let us assume that Ω is *bounded*, a very reasonable assumption since the CCD sensors have finite size. In this case, it is well known that Hamilton-Jacobi equations, in particular the SFS equation

$$-e^{-2u(x)} + J(x)\sqrt{f^2|\nabla u(x)|^2 + (\nabla u(x)\cdot x)^2 + Q(x)^2} = 0, \quad \forall x \in \Omega, \tag{15}$$

do not have a unique (discontinuous) viscosity solution [34, 3, 2]. To overcome this difficulty we need to add some a priori. In the viscosity framework, the authors generally add boundary conditions. The main classical boundary conditions are Dirichlet's, Neumann's [34, 3, 2] or Soner's state contraints [58, 9]. For the Shape from Shading problem, the authors generally consider *Dirichlet boundary conditions* [56, 19, 20, 53, 49, 51, 48]. With such boundary conditions, equation (15) becomes

$$\begin{cases} -e^{-2u(x)} + J(x)\sqrt{f^2|\nabla u(x)|^2 + (\nabla u(x)\cdot x)^2 + Q(x)^2} = 0, & \forall x \in \Omega, \\ u(x) = \varphi(x), & \forall x \in \partial\Omega, \end{cases} \tag{16}$$

where φ is a real continuous function defined on $\partial\Omega$. In this case, the following theorem ensures the uniqueness of the (discontinuous) viscosity solution.

[12] In the SFS problem, we rarely know the values of the solution on the boundary of the image.
[13] They consider C^2 surfaces with second order derivatives satisfying some properties: for example, Kimmel and Bruckstein [29] consider surfaces represented by Morse functions (with non-degenerate Hessians).

Theorem 1 [14] *Let Ω be bounded and smooth enough*[15]*, and $H : \Omega \times \mathbb{R}^2 \times \mathbb{R}^2 \mapsto \mathbb{R}$, continuous. If φ is continuous and if the hypotheses* (H1)-(H2) *and the boundary hypotheses* (H3)-(H4)-(H5) *(described below) hold, then we have a strong uniqueness property for equation*

$$\begin{cases} H(x, u(x), \nabla u(x)) = 0, & \forall x \in \Omega, \\ u(x) = \varphi(x), & \forall x \in \partial\Omega \end{cases} \tag{17}$$

(in the discontinuous viscosity sense) on Ω .

Let us recall that the *strong uniqueness* property (on a subset D of Ω) is the following:

If u and v are a (discontinuous) viscosity subsolution and supersolution, respectively, then

$$u \leq v \text{ on } D$$

Of course, the strong uniqueness property involves the uniqueness of the (discontinuous) viscosity solution.

Let us recall that the set of classical solutions is a subset of the (discontinuous) viscosity solutions. So the uniqueness of the (discontinuous) viscosity solution implies the uniqueness of the solution in the classical sense. Let us also recall that the strong uniqueness property involves the continuity of the (discontinuous) viscosity solution. Finally, note that in theorem 1, the strong uniqueness holds on Ω and not on $\overline{\Omega}$.
The hypotheses (H1) and (H2) are:

(H1) $H(x, u, p) - H(x, v, p) \geq \gamma_R(u - v), (\gamma_R > 0)$
for all $x \in \Omega$, $-R \leq v \leq u \leq R$, and $p \in \mathbb{R}^2$ $(\forall 0 < R < +\infty)$.

(H2) $|H(x, u, p) - H(y, u, p)| \leq m_R(|x - y|(1 + |p|))$
for all $x, y \in \Omega$, $-R \leq u \leq R$ and $p \in \mathbb{R}^2$,
where $m_R(t) \longrightarrow 0$ when $t \to 0$.

The boundary hypotheses (H3), (H4) and (H5) are the following:
There exists a subset Γ of $\mathbb{R}^2$ which is a neighborhood of $\partial\Omega$ such that

(H3) *for all $0 < R < +\infty$, there exists $m_R(t) \longrightarrow 0$ when $t \to 0$ such that*

$$|H(x, u, p) - H(x, u, q)| \leq m_R(|p - q|)$$

for all $x \in \Gamma$, $-R \leq u \leq R$ and $p, q \in \mathbb{R}^2$.

(H4) *for all $0 < R < +\infty$, there exists $C_R > 0$ such that*

$$H(x, u, p + \lambda n(x)) \leq 0 \Longrightarrow \lambda \leq C_R(1 + |p|),$$

for all $(x, u, p) \in \Gamma \times [-R, R] \times \mathbb{R}^2$.

(H5) $\forall R_1, R_2 \in \mathbb{R}^{+*}$,

$$H(x, u, p - \lambda n(x)) \longrightarrow +\infty \quad \text{when } \lambda \longrightarrow +\infty,$$

uniformly for (x, u, p) in $\Gamma \times [-R_1, R_1] \times B(0, R_2)$.

Application of theorem 1 to the SFS Hamiltonian H_F

- The hypothesis (H1) holds for H_F, for all brightness image I. In effect, for $-R \leq v \leq u \leq R$ we have:

$$\begin{aligned} H_F(x, u, p) - H_F(x, v, p) &= -e^{-2u} + e^{-2v} \\ &= 2(u - v)e^{-2c} \quad \text{(for some } c \in [v, u]\text{; by Taylor's expansion with remainder)} \\ &\geq 2(u - v)e^{-2R} \\ &\geq \gamma_R(u - v); \end{aligned}$$

  where $\gamma_R = 2e^{-2R} > 0$.

[14] See theorem 4.5 and corollary 4.1 of Barles' book [3].
[15] $\Omega \in W^{2,\infty}$.

- About hypothesis (H2), we write:

$$|H_F(x,u,p) - H_F(y,u,p)| = |H_C(x,p) - H_C(y,p)|.$$

Let us denote T_p the function defined by $\quad T_p : \Omega \to \mathbb{R} : x \mapsto H_C(x,p).$
In appendix A, we prove the

Lemma 1 *If J is differentiable on the bounded set Ω and if for all x in Ω, $|\nabla J(x)|$ and $J(x)$ are upper bounded, then for all $p \in \mathbb{R}^2$, the function T_p is Lipschitz continuous with a Lipschitz' constant of the form $\alpha(1+|p|)$ (α does not depend on p).*

  - Thus, as soon as for all x of Ω, $|\nabla J(x)|$ and $J(x)$ are bounded, lemma 1 involves that for all x and y in Ω, for all u s.t. $-R \leq u \leq R$ and for all p in $\mathbb{R}^2$, we have

$$|H_F(x,u,p) - H_F(y,u,p)| \leq \alpha|x-y|(1+|p|).$$

    That is to say (H2) holds with $m_R(t) = \alpha t$.
  - Since Ω *is bounded* (this involves in particular that $\forall x \in \Omega,\ Q(x) \geq \delta > 0$), one can verify easily that if the intensity image

$$I \text{ is differentiable and } I \text{ and } \nabla I \text{ are bounded on } \Omega,$$

    then $|\nabla J(x)|$ and $J(x)$ are bounded and so (H2) holds.

- For all x in Γ, let us consider the function $R^x : \mathbb{R}^2 \to \mathbb{R} : p \mapsto J(x)\sqrt{f^2|p|^2 + (x\cdot p)^2 + Q(x)^2}$.
  One can verify that for all $p \in \mathbb{R}^2$, $\quad |\nabla R^x(p)| \leq J(x)\sqrt{f^2+|x|^2}$. If the intensity image

$$I \text{ is upper bounded on a bounded neighborhood } \Gamma \text{ of } \partial\Omega,$$

  then $J(x)$ and so $J(x)\sqrt{f^2+|x|^2}$ are also upper bounded on Γ. Therefore $|\nabla R^x(p)|$ is bounded independently of x and p. The reader will conclude easily that, as soon as the intensity image I is upper bounded, the hypothesis (H3) holds.

- Let us assume that there exists a neighborhood Γ of $\partial\Omega$ and $\delta > 0$ such that

$$\forall x \in \Gamma, \quad \delta \leq I(x).$$

  For all $R > 0$ and for all (x,u,p) in $\Gamma \times [-R,R] \times \mathbb{R}^2$, we have

$$H_F(x,u,p) \geq -e^{2R} + \delta f^3|p|.$$

  Therefore $H_F(x,u,p)$ is coercive[16] in p uniformly with respect to $x \in \Gamma$ and $u \in [-R,R]$. Therefore hypotheses (H4) and (H5) are verified.

To summarize, as soon as I is differentiable and such that there exist $\delta > 0$ and M verifying $\delta \leq I(x) \leq M$ and $|\nabla I(x)| \leq M$ (for all x in a bounded neighborhood of Ω) then the Shape From Shading equation (16) has a unique (discontinuous) viscosity solution. In other words, if we know on the boundary of the image the depth of the surface which has produced the image, we are able to recover uniquely this surface. This surface corresponds to the viscosity solution of (16). Let us emphasize that this result holds independently of the local properties of the original surface. More precisely, this result holds even if the function u representing the original surface has local minima and maxima on Ω. This is in contrast with the difficulties encountered with all the other classical SFS equations presented in [52, 48]. In effect, for the other classical SFS equations, the local minima and maxima[17] of u create singular points. So, even though we know the values of the solution on $\partial\Omega$, the problem is still ill-posed.

In particular some concave/convex ambiguities can appear, see section 1. In order to recover a "global solution" [41, 31] we need to introduce some extra regularity hypotheses (we must consider at least C^2 solutions with nondegenerate Hessians, but let us recall that in practice such smooth solutions never exist) and to come

[16] i.e. $\lim_{p\to+\infty} H_F(x,u,p) = +\infty$ uniformly with respect to $x \in \Gamma$ and $u \in [-R,R]$.

[17] In fact, we must consider the local minima and maxima of $u - \psi$, where ψ is an adequate subsolution, see [47]. For most of the SFS Hamiltonians, an adequate subsolution ψ is the null function.

up with a (very difficult) classification of the singular points [38]. Finally, if we want to characterize or compute a viscosity solution of such degenerate equations, we require the knowledge of the solution at the points of the local minima, see theorem 6 of [47]. With our new modeling this kind of difficulty completely disappears.

In [52, 47, 50] we have shown that the idea of *state contraints* provides a more convenient notion of boundary conditions than Dirichlet's or Neumann's[18]. Let us recall that the "state contraint" is a boundary condition which is reduced to

$$H(x, u(x), \nabla u(x)) \geq 0 \qquad \text{on } \partial\Omega,$$

in the viscosity sense (see for example [3, 9]) and that this constraint corresponds to the Dirichlet's conditions

$$\forall x \in \partial\Omega, \quad u(x) = \varphi(x) \quad \text{with } \varphi(x) = +\infty$$

in the viscosity sense. In the sequel we will write this constraint

$$u(x) = +\infty, \quad \forall x \in \partial\Omega.$$

As we explain in [47], the interest of the notion of state constraints is twofolds. 1) In contrast with the Dirichlet and Neumann boundary conditions, the state constraints do not require any data. Let us recall that the Dirichlet (respectively, Neumann) boundary conditions require the knowledge of the exact values of the solution (respectively, the exact values of $\nabla u(x) \cdot n(x)$, where $n(x)$ is the unit inward normal vector to $\partial\Omega$ at the point x) on the boundary of the image. This is quite unrealistic because in the Shape from Shading problem, we rarely have such data at our disposal. 2) The notion of state constraints provides a relevant solution as soon as the image is obtained from a surface represented by u verifying that for all $x \in \partial\Omega$,

$$H(x, u, \xi) \geq 0, \quad \forall \xi \in D^- u(x), \tag{18}$$

see [47], for more details and the proof of the fact that a function u verifies the constraint (18) as soon as

$$\nabla_p H(x, u, \nabla u(x)) \cdot n(x) < 0.$$

For the Hamiltonian H_F, a function u verifies the constraint (18) as soon as $-f_c(x, \nabla u(x)) \cdot n(x) < 0$ (where f_c is defined below in section 5.1), i.e. as soon as

$$\nabla u(x) \cdot [{}^t Dil_x n(x)] < 0. \tag{19}$$

Since in this case the eigen values of Dil_x are strictly positive, the previous assumption holds roughly when $u(x)$ "increases when x tends to $\partial\Omega$".

Remark: The reader may wonder at this stage how constraining this condition really is. It is in fact not a strong constraint since for example, as soon as the image to be processed contains an object of interest in front of a background, the condition is satisfied in a neighbourhood of the object where $u(x)$ increases rapidly.

In order to prove the uniqueness of the solution in the case of state constraints, we have the theorem[19]

Theorem 2 *Let Ω be bounded and smooth enough[20], and $H : \Omega \times \mathbb{R}^2 \times \mathbb{R}^2 \mapsto \mathbb{R}$, continuous. If the hypotheses* (H1)-(H2) *hold and the boundary hypotheses* (H3)-(H4) *hold, then we have a strong uniqueness result for equation*

$$\begin{cases} H(x, u(x), \nabla u(x)) = 0, & \forall x \in \Omega, \\ u(x) = +\infty, & \forall x \in \partial\Omega \end{cases}$$

(in the discontinuous viscosity sense) on Ω.

[18] Let us recall that, already in [16], Dupuis and Oliensis have introduced some similar tools in the case of the C^1 solutions. Also in [35], Lions, Rouy and Tourin used the notion of state constraint for dealing with occluding contours.

[19] Theorem 4.6 of Barles' book [3].

[20] $\Omega \in W^{2,\infty}$.

By using theorem 2, we prove (as we have done for theorem 1) that the Shape From Shading equation

$$\begin{cases} -e^{-2u(x)} + J(x)\sqrt{f^2|\nabla u(x)|^2 + (\nabla u(x)\cdot x)^2 + Q(x)^2} = 0, & \forall x \in \Omega, \\ u(x) = +\infty, & \forall x \in \partial\Omega \end{cases} \tag{20}$$

has a unique (discontinuous) viscosity solution, as soon as $\delta < I(x) < M$ and $|\nabla I(x)| \leq M$. Thus we have a unique solution of (15) without requiring boundary data (as must be done with classical Neumann or Dirichlet boundary conditions). This solution corresponds to the actual surface producing the image as soon as this surface roughly increases when x gets close to the boundary of the image[21]. If this condition does not hold the resulting solution corresponds to the actual surface on the largest subset Θ of Ω for which (19) holds on $\partial\Theta$. As in the case of Dirichlet boundary conditions (theorem 1), let us emphasize that this uniqueness result and the correspondence of the solution with the actual surface hold even when the actual surface has local minima and maxima on Ω. In particular, we do not need to impose constraints at the singular points[22]. In other words the concave/convex ambiguities linked to the presence of the singularities completely disappear. Finally, if we know a priori that the original surface "increases" toward $\partial\Omega$ then the SFS problem is completely well-posed and there are no ambiguities. Of course, this conclusion does not hold for all the other classical SFS equations.

Remarks:

1. We have discussed the uniqueness of the solution of the SFS equations (16) and (20) but we have not considered the problem of the *existence of a solution*. In fact, using some stability results, we prove below that *equations (16) and (20) always have a solution*. In particular, thanks to the strong uniqueness result, we prove in section 5.3.3 that the solutions of the schemes we propose in section 5.3 converge toward a function which is a (discontinuous) viscosity solution of (16) (or (20), see section 5.2).

2. In large segments of the Shape from Shading literature, the authors state that the Shape from Shading problem is ill-posed and suggest that in order to solve it (numerically and/or theoretically) one has to resort to regularization. For example,

   (a) the minimization approaches [26, 15] add regularization terms in the SFS equations.

   (b) Oliensis and Dupuis [41, 16] need regularity hypotheses for characterizing a "global solution". They work in a set of constrained C^2 solutions.

   Contrary to this previous work, we prove in this paper that regularization is not required for ensuring the well-posedness of the SFS problem and for computing a numerical approximation of its solution. In particular,we can characterize nonsmooth solutions and we do not need to add regularization terms in the equations.

5 A provably convergent numerical method

In [36, 37], Okatani and Deguchi describe a numerical method based on the propagation of the equal-distance contours. As Bruckstein and Kimmel [8, 31] for the Eikonal equation, they design an evolution equation and propose to solve it by using a level-set method [43, 42, 57]. Although the method of Okatani and Deguchi is rigorous, it suffers from an important drawback because it requires an *initial equal-distance contour* and uses the *distance function of this contour*. The consequences are twofolds. First, it decreases the applicability of the method since such data (initial equal-distance contour and distance function of this contour) is usually not available. Second because these data, when available, are noisy they in fact may perturb the reconstruction! In effect, as we show in section 4, in the modeling framework of this paper (pinhole camera and light source located at the optical center, considering the attenuation term in $1/r^2$) the Shape from Shading problem is well posed[23]. Also, the characterization of the solution (and therefore its computation) does not require additional data. Let us note that when the initial equal-distance contour and distance function of this contour are exact, the numerical solution returned by the algorithm of Okatani and Deguchi is an approximation of the solution of equation (20) (equation completed with the state constraints). Nevertheless, when the imposed initial data contain errors, the reconstructed surface does not correspond with the solution of (20), neither with a solution

[21] The exact condition is the condition (19).
[22] Let us recall that the notion of singular points does not have sense in this setup!
[23] Here, we consider the SFS problem with state constraints on the boundary of the image.

of (16), for some φ. This kind of difficulties shows the interest of the theoretical analyses such as those presented in section 4.

We next propose a new numerical method. Contrary to [36, 37] it does not require an initial equal-distance contour. Moreover, our method is provably convergent: We prove that our numerical schemes are *stable, consistent* and that *their solutions converge toward the unique viscosity solution* of the problem. Let us note that Okatani and Deguchi do not even consider such questions whose practical importance should not be underestimated because, for example, they allow to certify algorithms, to guarantee their robustness and to describe their limitations...

From another point of view (although we have not implemented their method and hence have not made comparison tests), our numerical method *based on control theory* (and computing directly the solution of the *stationary equation*) is most probably much more efficient than theirs that solves an *evolution equation* by a *level-sets method.*

In the following we first describe a control formulation of the Hamiltonian H_F (section 5.1) and we explain how to deal with the boundary conditions (section 5.2). From this control formulation of H_F we design two monotonous approximation schemes and we prove their stability, consistence and convergence (section 5.3). Finally, we propose numerical algorithms which compute numerical approximations of the solutions of our new schemes (section 5.4).

5.1 Control formulation of the Hamiltonian H_F

Let us consider the function $H_C : \Omega \times \mathbb{R}^2 \mapsto \mathbb{R}^2$ given by:

$$H_C(x,p) = J(x)\sqrt{f^2|p|^2 + (p\cdot x)^2 + Q(x)^2}.$$

We therefore have

$$H_F(x,u,p) = -e^{-2u} + H_C(x,p).$$

In [52, 51, 48], Prados and Faugeras describe a "generic" SFS Hamiltonian H_g we recall here:

$$H_g(x,p) = \tilde{H}_g(x, A_x p + \overrightarrow{v_x}) + \overrightarrow{w_x}\cdot p + c_x,$$

with $\tilde{H}_g(x,q) = \kappa_x\sqrt{|q|^2 + K_x^2}$,

- $\kappa_x > 0$ and $K_x \geq 0$,
- $A_x = D_x\ R_x$, where
  - $D_x = \begin{pmatrix} \mu_x & 0 \\ 0 & \nu_x \end{pmatrix}$, $\mu_x, \nu_x \neq 0$,
  - if $x \neq 0$, R_x is the rotation matrix $R_x = \begin{pmatrix} \cos\theta & \sin\theta \\ -\sin\theta & \cos\theta \end{pmatrix}$; where $\cos\theta = \frac{x_2}{|x|}$ and $\sin\theta = -\frac{x_1}{|x|}$,
  - if $x = 0$, $R_x = Id_{2\times 2}$;
- $\overrightarrow{v_x}, \overrightarrow{w_x} \in \mathbb{R}^2$,
- $c_x \in \mathbb{R}$.

As in appendix B of [48], we prove that H_C is the particular case of H_g corresponding to:

$$\begin{aligned} \mu_x &= f & \nu_x &= \sqrt{f^2 + |x|^2} \\ \kappa_x &= J(x) & K_x &= \sqrt{\frac{f^2}{f^2+|x|^2}} \quad (\ = Q(x)\ ) \\ \overrightarrow{w_x} &= 0 & \overrightarrow{v_x} &= 0 \\ c_x &= 0. \end{aligned}$$

Therefore we can use the control formulation of H_g detailed in [51] or in section 3.3.2 of [48] (pages 23-24):

$$H_g(x,p) = \sup_{a\in\bar{B}_2(0,1)} \{-f_g(x,a)\cdot p - l_g(x,a)\}, \tag{21}$$

with

$$\begin{aligned} f_g(x,a) &= -\ [\ Dil_x a + \overrightarrow{w_x}\ ], \\ l_g(x,a) &= -\ [\ K_x \kappa_x \sqrt{1-|a|^2} + \kappa_x ({}^t R_x \overrightarrow{v_x}) \cdot a + c_x], \end{aligned}$$

where $Dil_x = \kappa_x\ {}^t R_x D_x R_x$.
If we denote f_c and l_c the functions f_g and l_g associated with H_C, we have

$$H_F(x,u,p) = -e^{-2u} + \sup_{a \in \bar{B}_2(0,1)} \{ -f_c(x,a) \cdot p - l_c(x,a) \} \tag{22}$$

where

$$\begin{aligned} f_c(x,a) &= -Dil_x a, \\ l_c(x,a) &= -I(x) f^2 \sqrt{1-|a|^2}. \end{aligned} \tag{23}$$

5.2 Management of the boundary conditions

Exactly as in section 7.1 of [47], we prove that the state contraints can always be rewritten as Dirichlet boundary conditions. The main argument of the proof is based on the fact that all the viscosity solutions of (20) are bounded by the same constant (see lemma 3 of appendix A). More precisely, we prove that the discontinuous viscosity solution of (20) (equation with state contraints) coincides with the discontinuous viscosity solution of (16) (equation with Dirichlet's contions) with $\varphi(x) = M$ $(\forall x \in \partial\Omega)$. In practice we therefore always consider Dirichlet boundary conditions. If we happen to know the values of the solution on $\partial\Omega$ we constrain φ accordingly otherwise we choose φ to be a "large" constant.

5.3 Two new approximation schemes

In this section, we propose two finite difference approximation schemes on a regular mesh. The reader unfamiliar with the notion of approximation schemes can refer to chapter 4 of the research report [48]. Note that the schemes we describe in this paper can be easily extended to irregular meshes (see [46]).

Let us just recall that an approximation scheme is a functional equation of the form

$$T(\rho, x, u) = 0 \qquad \forall x \in \overline{\Omega};$$

where $T : \mathcal{M} \times \overline{\Omega} \times B(\overline{\Omega}) \to \mathbb{R}$, $\mathcal{M} = \mathbb{R}^+ \times \mathbb{R}^+$ and $B(D)$ is the space of bounded functions defined on a set D. $\rho = (h_1, h_2) \in \mathcal{M}$ defines the size of the mesh that is used in the corresponding numerical algorithms. Moreover, following [4], we use the representations S of a scheme T as

$$S(\rho, x, u(x), u) = 0 \qquad \forall x \in \overline{\Omega},$$

where

$$\begin{array}{rccc} S: & \mathcal{M} \times \overline{\Omega} \times \mathbb{R} \times B(\overline{\Omega}) & \longrightarrow & \mathbb{R} \\ & (\rho, x, t, u) & \longmapsto & S(\rho, x, t, u). \end{array}$$

Note that a representation of a scheme is also a scheme. It is in effect a way to simplify computations, see [48].

In practice Ω is bounded and we deal with PDEs with Dirichlet boundary conditions[24]. We must therefore consider "schemes with Dirichlet boundary conditions", i.e. schemes such that:

$$S(\rho, x, t, u) = \begin{cases} \tilde{S}(\rho, x, t, u) & \text{if } x \in \Omega^\rho, \\ t - \varphi(x) & \text{if } x \in \flat\Omega^\rho, \end{cases} \tag{24}$$

where

$$\Omega^\rho = \{ x \in \Omega \mid \forall i \in \{1,2\},\ x \pm h_i \overrightarrow{e_i} \in \overline{\Omega} \} \quad \text{and} \quad \flat\Omega^\rho = \overline{\Omega} - \Omega^\rho.$$

Note that we assume in (24) that we have extended φ continuously to $\flat\Omega^\rho$.

[24] Let us recall that, since all solutions of our SFS PDE are bounded, the state contraints can be rewritten as Dirichlet boundary conditions.

5.3.1 Design of the approximation schemes

There exists more or less only one method ensuring the convergence of the solutions of schemes toward viscosity solutions, i.e. the one presented by Barles and Souganidis in [4]. This method requires the monotonicity of the scheme; this is why we design a monotonous scheme in the sequel. We recall the definition:

Definition 1 (monotonicity) *The scheme $S(\rho, x, u(x), u) = 0$ defined on $\overline{\Omega}$ is monotonous if $\forall \rho, \forall x \in \overline{\Omega}, \forall t \in \mathbb{R}$ and $\forall u, v \in B(\overline{\Omega})$,*

$$u \leq v \quad \Longrightarrow \quad S(\rho, x, t, u) \geq S(\rho, x, t, v)$$

(that is to say: the scheme is nonincreasing with respect to u)

The reader unfamiliar with monotonous schemes can refer to [48, 4]. For proving the stability of our scheme, we can apply theorem 8 of [48]. This requires that the function $t \mapsto S(\rho, x, t, u)$ is nondecreasing.

In [48], we have proposed to approximate $H_C(x, \nabla u(x))$ by:

$$\begin{aligned} H_C(x, \nabla u(x)) \;\approx\; & \sup_{a \in A} \left\{ \sum_{i=1}^{2} (-f_i(x,a)) \frac{u(x) - u(x + s_i(x,a) h_i \overrightarrow{e_i})}{-s_i(x,a) h_i} - l_c(x,a) \right\} \\ & = \sup_{a \in A} \left\{ \left(\sum_{i=1}^{2} \frac{|f_i(x,a)|}{h_i} \right) u(x) - \sum_{i=1}^{2} \frac{|f_i(x,a)|}{h_i} u(x + s_i(x,a) h_i \overrightarrow{e_i}) - l_c(x,a) \right\}, \end{aligned} \tag{25}$$

where $f_i(x,a)$ is the i^{th} componant of $f_c(x,a)$, where $s_i(x,a)$ is its sign and where $A = \bar{B}(0,1)$ is the closed unit ball.
We can therefore approximate $H_F(x, u(x), \nabla u(x))$ by:

$$\begin{aligned} H_F(x, u(x), \nabla u(x)) \;\approx\; & - e^{-2\ u(x)} \\ & + \sup_{a \in A} \left\{ \left(\sum_{i=1}^{2} \frac{|f_i(x,a)|}{h_i} \right) u(x) - \sum_{i=1}^{2} \frac{|f_i(x,a)|}{h_i} u(x + s_i(x,a) h_i \overrightarrow{e_i}) - l_c(x,a) \right\}. \end{aligned} \tag{26}$$

So, we can formulate a first representation (with Dirichlet boundary conditions) S_{impl} based on the function:

$$\begin{aligned} & \tilde{S}_{impl}(\rho, x, t, u) \\ & \quad = -e^{-2\ t} + \sup_{a \in A} \left\{ \left(\sum_{i=1}^{2} \frac{|f_i(x,a)|}{h_i} \right) t - \sum_{i=1}^{2} \frac{|f_i(x,a)|}{h_i} u(x + s_i(x,a) h_i \overrightarrow{e_i}) - l_c(x,a) \right\} \\ & \quad = -e^{-2\ t} + \sup_{a \in A} \left\{ \sum_{i=1}^{2} (-f_i(x,a)) \frac{t - u(x + s_i(x,a) h_i \overrightarrow{e_i})}{-s_i(x,a) h_i} - l_c(x,a) \right\}. \end{aligned} \tag{27}$$

Notes:

1. The function $t \mapsto S_{impl}(\rho, x, t, u)$ is obviouly nondecreasing. The representation S_{impl} is also clearly monotonous.
2. This first representation provides a very fast algorithm. It is implicit but can be made explicit by using differential calculus.

As in [51, 48], we can provide another (more explicit) representation. We multiply (27) by a fictitious time increment $\Delta\tau$ ($\Delta\tau > 0$ can depend on x, $\Delta\tau = \Delta\tau(x)$), add $u(x)$ and $-u(x)$ and obtain:

$$\begin{aligned} & \hat{S}(\rho, x, u(x), u) = u(x) - \Delta\tau e^{-2\ u(x)} \\ & \quad + \sup_{a \in A} \left\{ - \left(1 - \Delta\tau \sum_{i=1}^{2} \frac{|f_i(x,a)|}{h_i} \right) u(x) - \Delta\tau \sum_{i=1}^{2} \frac{|f_i(x,a)|}{h_i} u(x + s_i(x,a) h_i \overrightarrow{e_i}) - \Delta\tau l_c(x,a) \right\}. \end{aligned} \tag{28}$$

We can also choose a second representation (with Dirichlet boundary conditions) S_{semi} based on the function:

$$\begin{aligned}\tilde{S}_{semi}(\rho,x,t,u) &= t-\Delta\tau e^{-2t}\\ &+\sup_{a\in A}\left\{-\left(1-\Delta\tau\sum_{i=1}^{2}\frac{|f_i(x,a)|}{h_i}\right)u(x)-\Delta\tau\sum_{i=1}^{2}\frac{|f_i(x,a)|}{h_i}u(x+s_i(x,a)h_i\overrightarrow{e_i})-\Delta\tau l_c(x,a)\right\}\\ &= t-\Delta\tau e^{-2t}-u(x)+\Delta\tau\sup_{a\in A}\left\{\sum_{i=1}^{2}(-f_i(x,a))\frac{u(x)-u(x+s_i(x,a)h_i\overrightarrow{e_i})}{-s_i(x,a)h_i}-l_c(x,a)\right\}. \quad (29)\end{aligned}$$

Note: The function $t\mapsto S_{semi}(\rho,x,t,u)$ is obviously nondecreasing. But the representation S_{semi} is not always monotonous.

Let us denote now a_0 the optimal control[25] of (25). For all x such that $a_0\neq 0$, let us introduce

$$\Delta\tau_{opt}=\left(\sum_{i=1}^{2}\frac{|f_i(x,a_0)|}{h_i}\right)^{-1}.$$

Remark: a_0 and the optimal $\Delta\tau_{opt}$ depend on x.

The reader will easily verify that *the scheme $S_{semi}(\rho,x,u(x),u)=0$ is monotonous iff $\Delta\tau\leq\Delta\tau_{opt}$*. Let us mention that the larger the "parameter" $\Delta\tau$, the faster the convergence. When we choose $\Delta\tau=\Delta\tau_{opt}$, $\tilde{S}_{semi}$ can be rewritten [26]:

$$\begin{aligned}\tilde{S}^{opt}_{semi}(\rho,x,t,u) &= t-\frac{1}{\sum_{j=1}^{N}|f_j(x,a_0)|/h_j}e^{-2t}\\ &-\sum_{i=1}^{2}\frac{|f_i(x,a_0)|/h_i}{\sum_{j=1}^{2}|f_j(x,a_0)|/h_j}\,u(x+s_ih_i\overrightarrow{e_i})-\frac{1}{\sum_{j=1}^{2}|f_j(x,a_0)|/h_j}\,l_c(x,a_0). \quad (30)\end{aligned}$$

In summary the representation S_{impl} is always monotonous, the representation S_{semi} is monotonous iff $\Delta\tau\leq\Delta\tau_{opt}$, the representation S^{opt}_{semi} is always monotonous and it is the most effective monotonous representation of the form S_{semi}.

Remark: The reader will verify that the numerical method we describe here can be applied to all equations of the form:

$$G(u(x)+H(x,\nabla u(x))=0,$$

where G is a nondecreasing function and H is a convex Hamiltonian (with respect to p).

5.3.2 Stability of our approximation schemes

Thanks to the monotony properties we can apply theorem 8 of [48] which proves the stability of our new schemes (see [48] for the definition of the stability). Let us recall that an approximation scheme is "(uniformly) stable" when it has (uniformly) bounded solutions (see [4, 48]).

Remark: By construction $S_{semi}(\rho,x,u(x),u)=\Delta\tau S_{impl}(\rho,x,u(x),u)$. So the schemes S_{semi} and S_{impl} have exactly the same subsolutions, supersolutions and solutions. Therefore, S_{semi} is (uniformly) stable iff S_{impl} is (uniformly) stable.

The following proposition ensures the stability of our schemes.

Proposition 1 *If there exist δ and M such that $\forall x\in\overline{\Omega}$, $M\geq I(x)\geq\delta>0$, then the schemes S_{impl} and S_{semi} are uniformly stable.*

PROOF.

- The hypotheses (H16), (H17) and (H18) of [48] are clearly satisfied.

[25] The a in A for which the maximum of (25) is reached

[26] a_0 does not depend on $\Delta\tau$.

- The proof that hypothesis (H19) of [48] holds is the same as the proof detailed in section 4.3.2 of [48] ensuring that (H19) holds for the implicit scheme (see in particular proposition 4 of [48]).

- Let us assume that $I(x)$ is bounded by M on $\overline{\Omega}$. This implies that

$$\sup_{a\in A,\ x\in\overline{\Omega}} \{-l_c(x,a)\} \leq Mf^2.$$

Considering equation (29) or (27), we see that, *for all constant function* u, we have:

$$\tilde{S}_{semi}(\rho,x,u(x),u) \quad = \quad \Delta\tau\tilde{S}_{impl}(\rho,x,u(x),u) \quad = \quad \Delta\tau\left(-e^{-2\ u(x)} + \sup_{a\in A}\{-l_c(x,a)\}\right).$$

Since $\lim_{u\to-\infty} -e^{-2\ u} = -\infty$, we can choose a constant function u such that

$$\forall x \in \overline{\Omega}, \quad -e^{-2\ u(x)} \leq -Mf^2.$$

For such a function u, we clearly have $\forall x \in \overline{\Omega}$

$$\tilde{S}_{semi}(\rho,x,u(x),u) \leq 0.$$

(of course, we also have, $\tilde{S}_{impl}(\rho,x,u(x),u) \leq 0$).
Modulo the subtraction of $\min\varphi(x)$ from u, we conclude that u is a subsolution of S_{semi} and S_{impl}. Therefore hypothesis (H20) of [48] holds for S_{semi} and S_{impl}, as soon as $I(x)$ is upper bounded by M on $\overline{\Omega}$.

- We now show that all the subsolutions of our schemes are uniformly bounded.
Let u be a subsolution of S_{impl} and S_{semi}.
For all $x \in \flat\Omega^\rho$,

$$u(x) \leq \varphi(x) \leq \max_{y\in\overline{\Omega}}\varphi(y).$$

Moreover, for all $x \in \Omega^\rho$, we have

$$-e^{-2\ u(x)} + \sup_{a\in A}\left\{\sum_{i=1}^{2}(-f_i(x,a))\frac{u(x)-u(x+s_i(x,a)h_i\overrightarrow{e_i})}{-s_i(x,a)h_i} - l_c(x,a)\right\} \leq 0.$$

In particular (for $a=0$)

$$-e^{-2\ u(x)} + \sum_{i=1}^{2}(-f_i(x,0))\frac{u(x)-u(x+s_i(x,0)h_i\overrightarrow{e_i})}{-s_i(x,0)h_i} - l_c(x,0) \leq 0.$$

Since $-l_c(x,0) = I(x)f^2$ and $f_c(x,0) = 0$, we have

$$-e^{-2\ u(x)} \leq -I(x)f^2.$$

If we assume $\forall x \in \overline{\Omega},\ I(x) \geq \delta > 0$, then for all x in $\overline{\Omega}$,

$$-e^{-2\ u(x)} \leq -\delta f^2.$$

Thus, as soon as $\forall x \in \overline{\Omega},\ I(x) \geq \delta > 0$, we conclude that all the subsolutions of the scheme S_{impl} and S_{semi} are uniformly upper bounded by

$$\max\{-\frac{1}{2}\ln(\delta f^2)\ ,\ \max_{y\in\overline{\Omega}}\varphi(y)\}$$

and so the hypothesis (H21) of [48] holds.

- We have proved that all the hypotheses of theorem 8 of [48] hold for the schemes S_{impl} and S_{semi}. This allows us to conclude that they are uniformly stable.

□

Remark: Using the fact that $I(x) \geq \delta > 0$ and $\lim_{u \to +\infty} -e^{-2\ u} = 0$, the reader will verify easily that all "large enough" constant functions are *supersolutions* of S_{impl} and S_{semi}. Therefore *hypothesis (H20') of [48] holds.* The proof that all supersolutions are uniformly lower bounded (hypothesis (H21') of [48]) is slightly more difficult:

PROOF. Let u be a supersolution. For each point $x \in \overline{\Omega}$, we can associated the grid $\mathcal{X}_x$:

$$\mathcal{X}_x := \left\{ x + \sum_{i=1..2} k_i h_i \overrightarrow{e_i} \mid (k_1, k_2) \in \mathbb{Z}^2 \right\} \cap \overline{\Omega}.$$

Since we have assumed that $\overline{\Omega}$ is bounded then $\mathcal{X}_x$ is a finite set. Therefore $u_{|\mathcal{X}_x}$ has a minimum. Let us denote

$$y_x = \text{argmin}_{y \in \mathcal{X}_x} u(y).$$

Thus for all $i = 1..2$, we have $u(y_x) - u(y_x + s_i(y_x, a) h_i \overrightarrow{e_i}) \leq 0$; so

$$\sup_{a \in A} \left\{ \sum_{i=1}^{2} |f_i(y_x, a)| \frac{u(y_x) - u(y_x + s_i(y_x, a) h_i \overrightarrow{e_i})}{h_i} - l_c(y_x, a) \right\} \leq \sup_{a \in A} \{-l_c(y_x, a)\} \leq I(y_x) f^2.$$

Since we have assumed that u is a supersolution, we have

$$S(\rho, y_x, u(y_x), u) \geq 0.$$

1. If $y_x \in \flat\Omega^\rho$ then
$$u(y_x) \geq \varphi(y_x) \geq \min_{y \in \overline{\Omega}} \varphi(y).$$

2. If $y_x \in \Omega^\rho$
$$\tilde{S}(\rho, y_x, u(y_x), u) \geq 0$$
then
$$-e^{-2\ u(y_x)} \geq -\sup_{a \in A} \left\{ \sum_{i=1}^{2} |f_i(y_x, a)| \frac{u(y_x) - u(x + s_i(y_x, a) h_i \overrightarrow{e_i})}{h_i} - l_c(y_x, a) \right\}.$$
Hence
$$-e^{-2\ u(y_x)} \geq -I(y_x) f^2.$$
If $\forall x \in \overline{\Omega},\ I(x) < M$, then
$$u(y_x) \geq -\frac{1}{2} \ln(M f^2).$$

Let us denote $B := \min\{-\frac{1}{2}\ln(Mf^2)\ ,\ \min_{y \in \overline{\Omega}} \varphi(y)\}$. Since $u(x) \geq u(y_x)$ (because $u(y_x)$ is the minimum of $u_{|\mathcal{X}_x}$) therefore $u(x) \geq B$. B being independent of x, we have $\forall x \in \overline{\Omega},\ u(x) \geq B$. B being also independent of ρ, we conclude that the supersolutions are uniformly lower bounded. Therefore *hypothesis (H21') of [48] holds.* □

The reader can verify that *hypothesis (H17') also holds.*

Therefore the schemes S_{impl} and S_{semi} are also *stable* when *starting from a supersolution* (see remark R16.3 of [48], pages 52-53). This remark is very important because it ensures the convergence of the associated algorithm when starting from a supersolution. In practice we have noticed that *the numerical algorithm converges* much faster toward the solution of the scheme *when we start from a supersolution than when we start from a subsolution*, see also chapter 7 of [48].

Remark: The (uniform) stability of the schemes S_{impl} and S_{semi} does not require regularity of the brigthness image I.

5.3.3 Convergence toward the viscostity solutions

In the previous section we have proved that the schemes S_{impl} and S_{semi} are uniformly stability. That is to say, for all fixed mesh size ρ, the schemes have solutions (i.e there exists of a function u s.t. $\forall x \in \overline{\Omega},\ S(\rho, x, u(x), u) = 0$) and all the solutions are bounded independently of ρ. In this section we prove furthermore that the solutions of these schemes converge toward the unique (discontinuous) viscosity solution of the considered equation ((16) or (20)), when the size of the mesh ρ vanishes.

First, by using proposition 7 of [48] the schemes S_{impl} and S_{semi} are consistent (following Barles and Souganidis's definition [4]) as soon as f_c and l_c are continuous on $A \times \overline{\Omega}$ and Lipschitz continuous with respect to $x \in \overline{\Omega}$ and l_c is bounded. More precisely, it is consistent as soon as the *brightness image I is Lipschitz continuous* (the expressions of f_c and l_c are detailed on page 15).

Now let us assume that Ω is bounded, that the brightness image I is Lipschitz continuous (hence upper bounded) and that there exists δ such that $\forall x \in \overline{\Omega}, I(x) \geq \delta > 0$, then by proposition 1, the schemes S_{impl} and S_{semi} are uniformly stable. By construction, these schemes are monotonous. Moreover we have just seen that they are consistent with the SFS equations (16) and (20). Finally, in section 4 we have proved that the strong uniqueness property holds on Ω. Therefore, we can apply

Theorem 3 (Convergence toward the viscosity solution - Theorem 10 of [48]) *Let S be a monotonous, uniformly stable and consistent[27] approximation scheme. Let us suppose that the strong uniqueness property is verified on a subset D of $\overline{\Omega}$. Then the solutions of the scheme S converge on D toward the viscosity solution of the considered equation when $\rho \to 0$.*

The solutions of the schemes S_{impl} and S_{semi} hence converge on Ω toward the unique viscosity solution of considered equation ((16) or (20)) when the mesh size vanishes.

Remark: It is worth noting that this result (theorem 3) also proves the existence of the viscosity solution of equation (16). More precisely, this theorem shows that, when the mesh size vanishes, the solutions of our schemes converge toward a function which is a (discontinuous) viscosity solution of equation (16) (equation with Dirichlet Boundary Conditions). Similarly combining section 5.2 with theorem 3 allows to prove the existence of a (discontinuous) viscosity solution of equation (20) (equation with state constraints).

5.4 A numerical algorithm

We now describe an algorithm that computes an approximation of the solutions of the scheme (29) for all $\rho > 0$. We also prove its convergence. It is important to keep in mind that the approximations computed by our algorithm converge toward solutions of the scheme but not toward the viscosity solution.

For a fixed $\rho > 0$, let us denote

- $x_k = (k_1 h_1, k_2 h_2)$ for k in $\mathbb{Z}^2$, $\qquad x_{ij} = (ih_1, jh_2)$ for $i, j \in \mathbb{Z}$,
- $Q := \{k \in \mathbb{Z}^2 \text{ such that } x_k \in \overline{\Omega}\}$.

We call "pixel" a point x_k in $\overline{\Omega}$. Since $\overline{\Omega}$ is bounded; therefore the number of pixels is finite. The following algorithm computes for all $k \in Q$ a sequence of approximations U_k^n of $u(x_k)$:

Algorithm 1

1. *Initialisation ($n = 0$):*
$$\forall k \in Q, \qquad U_k^0 = u_0(x_k),$$
where u_0 is a subsolution or a supersolution of the considered scheme.

2. *Choice of a pixel x_k and modification (step $n+1$) of U_k^n:*
Choose
$$U^{n+1} = \sup \{V = (V_l)_{l \in Q} \text{ such that } \forall l \neq k, \quad V_l = U_l^n \text{ and } S(\rho, x_k, V_k, V) = 0\}.$$
In other words, we choose U^{n+1} such that
$$\begin{cases} U_l^{n+1} = U_l^n \quad \text{if} \quad l \neq k, \\ U_k^{n+1} = \max \{\ t \mid S(\rho, x_k, t, U^n) = 0\ \}. \end{cases}$$

[27] Consistent with the considered equation.

3. Choose the next pixel x_k in such a way that all pixels are regularly visited and go back to 2.

All the remarks of chapter 6 of [48] about paths and speed of convergence still hold for this new method (the schemes described in the previous section are monotonous schemes of the form $S(p, x, u^p(x), u^p) = 0$). For example, in practice, for an optimal velocity, we should start from a supersolution. Also, since all the hypotheses of theorem 8 of [48] (as well as the equivalent hypotheses adapted to supersolutions) hold for our two representations S_{impl} and S_{semi}, theorem 11 of [48] ensures that the approximations converge toward the solutions of our new schemes. Moreover, let us remind that, when the intensity image is discontinuous, the viscosity solutions theory does not apply yet, but we can prove that the numerical approximation computed by our algorithms converge.

5.4.1 Details of the step 2 for the semi-implicit algorithm

Step 2 requires two stages. We suppose that we work with pixel x_{ij} and for simplicity we drop wht upper index n, i.e. write U_{ij} instead of U_{ij}^n.

1. First we need to compute:

$$M = \sup_{a \in A} \left\{ -f_c(x_{ij}, a) \cdot P_{U,i,j}^{s_1(x_{ij},a), s_2(x_{ij},a)} - l_c(x_{ij}, a) \right\},$$

with

$$P_{U,i,j}^{s_1,s_2} = \begin{pmatrix} \frac{U_{i,j} - U_{i+s_1,j}}{-s_1 h_1} \\ \frac{U_{i,j} - U_{i,j+s_2}}{-s_2 h_2} \end{pmatrix},$$

and where $s_i(x, a)$ is the sign of $f_i(x, a)$. To this end, we divide the set A into four subsets $A_{s_1,s_2} = \{a \in A \mid (s_1(x_{ij}, a), s_2(x_{ij}, a)) = (s_1, s_2)\}$, $s_1, s_2 \in \{\pm 1\}$

$$A = \bigcup_{s_1, s_2 = \pm 1} A_{s_1,s_2}$$

and we compute the optimal control $a_0^{s_1,s_2}$ for each subset:

$$a_0^{s_1,s_2} = arg \sup_{a \in A_{s_1,s_2}} \left\{ -f_c(x_{ij}, a) \cdot P_{U,i,j}^{s_1,s_2} - l_c(x_{ij}, a) \right\}.$$

This must be done carefully. In particular, we must separate the cases where $a_0^{s_1,s_2}$ verifies $f_i(x_{ij}, a_0^{s_1,s_2}) = 0$ for some $i \in \{1, 2\}$ (i.e $a_0^{s_1,s_2} \in \partial A_{s_1,s_2}$) and the cases where $a_0^{s_1,s_2} \in \mathrm{Int} A_{s_1,s_2}$. To simplify this step, we use convexity arguments and differential calculus. For more details, the reader is referred to [46]. Moreover, if we write

$$M_{s_1,s_2} = -f_c(x_{ij}, a_0^{s_1,s_2}) \cdot P_{U_{ij}}^{s_1(x_{ij}, a_0^{s_1,s_2}), s_2(x_{ij}, a_0^{s_1,s_2})} - l_c(x_{ij}, a_0^{s_1,s_2}),$$

it follows that $M = \max_{s_1,s_2 \in \{\pm 1\}} M_{s_1,s_2}$.

Remark: Various simple tricks (for example based on the fact that the intersection $\cap_{s_1,s_2 \in \{\pm 1\}} A_{s_1,s_2}$ is not empty) allow to decrease the computational complexity of this step, but because of space we do not detail them here. The interested reader will most probably discover very easily most of them...

2. Second, we need to solve with respect to t the equation

$$t - \Delta\tau e^{-2t} + c = 0, \tag{31}$$

where c is the constant coefficient:

$$c = -U_{i,j} + \Delta\tau \sup_{a \in A} \left\{ -f_c(x_{ij}, a) \cdot P_{U,i,j}^{s_1(x_{ij},a), s_2(x_{ij},a)} - l_c(x_{ij}, a) \right\} \tag{32}$$

$$= -U_{i,j} - \Delta\tau\ f_c(x_{ij}, a_0) \cdot P_{U,i,j}^{s_1(x_{ij},a_0), s_2(x_{ij},a_0)} - \Delta\tau\ l_c(x_{ij}, a_0) \tag{33}$$

(which is also equal to

$$c = -\Delta\tau_{opt}\ [\ f_c(x_{ij}, a_0) \cdot Q_{U,i,j}^{s_1(x_{ij},a_0), s_2(x_{ij},a_0)} + l_c(x_{ij}, a_0)\ ]$$

with $Q^{s_1,s_2}_{U,i,j} = (s_1 U_{i+s_1,j}/h_1, s_2 U_{i,j+s_2}/h_2)$, when $\Delta\tau = \Delta\tau_{opt}$).
For solving equation (31), we use Newton's method. This method can be easily improved by using some acceleration technique (see for example [6]). Let $g : \mathbb{R} \to \mathbb{R}$ be the C^∞ function defined by

$$g(t) = t - \Delta\tau e^{-2t} + c$$

and let $(t^k)_{k\in\mathbb{N}}$ be the sequence defined by:

$$\begin{array}{rcl} t^0 & = & U_{i,j}, \\ t^{k+1} & = & t^k - \frac{g(t^k)}{g'(t^k)}. \end{array} \tag{34}$$

Proposition 2 *For all $\Delta\tau > 0$ and c in $\mathbb{R}$, equation (31) has a unique solution $\bar{t}$. Also, the sequence designed by (34) converges toward this solution.*

PROOF. g is continuous, $\lim_{t\to-\infty} g(t) = -\infty$ and $\lim_{t\to+\infty} g(t) = +\infty$. So equation (31) has always a solution. For all t in $\mathbb{R}$, we have

$$g'(t) = 1 + 2\Delta\tau e^{-2t} > 1. \tag{35}$$

g is therefore strictly increasing and the solution of (31) is unique. Let us denote $\bar{t}$ this solution.

Lemma 2 $\forall k > 1$, $t^k \le t^{k+1} \le \bar{t}$.

By lemma 2, $(t^k)_{k>1}$ is an increasing and bounded sequence, hence convergent. By continuity of $h : r \mapsto r - \frac{g(r)}{g'(r)}$ the limit of $(t^k)_{k>1}$ is a fixed point of h, so it is equal to $\bar{t}$.

PROOF OF LEMMA 2. First let us assume that $t^1 \le \bar{t}$.
Proof by recursion:

(a) $t^1 \le \bar{t}$.

(b) let us assume that $t^k \le \bar{t}$. Since g is a nondecreasing function we have $g(t^k) \le 0$. By (35), $-\frac{g(t^k)}{g'(t^k)} \ge 0$. Therefore $t^{k+1} \ge t^k$.
Graphically, $(t^{k+1}, 0)$ is on the tangent to the graph of g at $(t^k, g(t_k))$. Since g is strictly concave[28], $(t^{k+1}, 0)$ is above the graph of g and so above $(t^{k+1}, g(t^{k+1}))$. Hence $g(t^{k+1}) \le 0$ and therefore $t^{k+1} \le \bar{t}$ (because g is strictly increasing).
In short: $t^k \le t^{k+1} \le \bar{t}$.

The proof that $t^1 \le \bar{t}$ is based on the same ideas. □

□

5.4.2 Examples of supersolutions of our schemes

In this section, we describe two examples of supersolutions of the schemes presented in section 5.3.
Let us recall that the implicit scheme (27) and the semi-implicit scheme (29) (and of course (30)) have exactly the same solutions, subsolutions and supersolutions.
We have the

Proposition 3 *The constant function $u_0 : \overline{\Omega} \to \mathbb{R}$ defined by*

$$u_0(x) = -\frac{1}{2}\ln\left(\delta f^2\right)$$

where $\delta = \min(I(x)) > 0$, and the function $v_0 : \overline{\Omega} \to \mathbb{R}$ defined by

$$v_0(x) = -\frac{1}{2}\ln\left(I(x) f^2\right) = -\left(\frac{1}{2}\ln I(x) + \ln f\right)$$

are two supersolutions of the implicit scheme (27).

[28] $g''(t) = -4\Delta\tau e^{-2t} < 0$.

PROOF. Let us consider the case of v_0. For all $x \in \overline{\Omega}$, we have

$$\tilde{S}_{impl}(\rho, x, v_0(x), v_0) = -e^{-2\ v_0(x)} + \sup_{a \in A} \left\{ \sum_{i=1}^{2} (-f_i(x,a)) \frac{v_0(x) - v_0(x + s_i(x,a) h_i \overrightarrow{e_i})}{-s_i(x,a) h_i} - l_c(x,a) \right\},$$

where A $= \bar{B}(0,1)$. Since $0 \in A$, $f(x,0) = 0$ and $l(x,0) = -I(x) f^2$, we have

$$\tilde{S}_{impl}(\rho, x, v_0(x), v_0) \geq -e^{-2\ v_0(x)} + I(x) f^2 = 0.$$

So v_0 is a supersolution of the scheme (27).
In the same way, we prove that u_0 is a supersolution of the scheme (27). □

6 Experimental results

Let us emphasize that in all the experiments that follow, *we have only imposed state constraints on the boundary of the images* $\partial\Omega$. In particular, we do *not* have imposed Dirichlet boundary conditions on $\partial\Omega$. Of course, we have not imposed Dirichlet boundary conditions at the singular points. Let us recall that in our framework, the notion of singular points does not make sense anymore! In other words, in these experiments *we have not used any boundary data.*

We have implemented the algorithm associated with the *optimal semi-implicit* approximation scheme. The reader familiar with the numerical methods presented in [48] will easily see that the implementation of this new semi-implicit algorithm is almost a direct extension of the implementation of the "generic" semi-implicit algorithm described in [48]. We only have to implement Newton's method detailed in subsection 5.4.1 in order to solve equation (31) and we need to slightly change the update step... We have not implemented yet the algorithm associated to the implicit scheme.
Since our new semi-implicit algorithm is *iterative*, to start the process we need an *initial surface* U_0. Of course, as usual, the choice of this initial surface is very important. As we show in section 5.4, starting from a supersolution ensures the convergence of the computed numerical approximations toward the solution of the associated scheme. In section 5.4.2, we have given two examples of supersolutions: the constant function

$$u_0(x) = -\frac{1}{2} \ln \left(\delta f^2 \right),$$

where $\delta = \min(I(x)) > 0$, and the function

$$v_0(x) = -\left(\frac{1}{2} \ln I(x) + \ln f \right).$$

Figure 7 displays the supersolution v_0 associated to image of the classical Mozart's face[29]. We have tested our

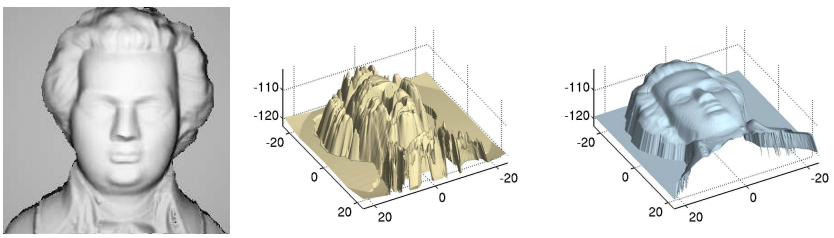

a) b) c)

a) Image; b) supersolution v_0 associated to the image a); c) solution (groundtruth).

Figure 7: Example of initial supersolution for the image of Mozart's Face.

algorithm with the two supersolutions. As the theory predicts, in both cases, we obtain the same numerical

[29] See Zhang et al. [66] (Computer Vision Lab. of the university of Central Florida).

solutions (i.e two extremely close solutions, with the same order of errors; the difference between the surfaces is invisible). But the number of iterations required for obtaining the convergence is very different. Indeed, starting from the supersolution v_0 is significatively faster than starting from the constant supersolution u_0. On average, if we start from u_0, the convergence is reached after around 500 iterations, when if we start from v_0, less than 60 iterations are sufficient (the number of iterations is reduced by one order of magnitude!). This result could be easily anticipated since the supersolution v_0 is very much closer to the solution than the supersolution u_0, as figure 7 shows. Figures 13 and 14 illustrate the difference of the evolutions in the two cases: when the algorithm starts from u_0 and when it starts from v_0. In other respects, let us note that exactly as for the algorithms presented in [48], it is clear that the implicit version of this algorithm will allow to reduce again the number of iterations by one order of magnitude (on average, the implicit algorithm should converge in less than 10 iterations). In the results displayed in the sequel, *n corresponds to the number of iterations.* Our algorithms being iterative, they also require a *stopping criterion.* We choose to stop the iterations when the difference between the successive reconstructions is negligible. In practice, we have fixed a thresholds of $s = 10^{-10}$ and we stop the process when

$$\frac{1}{NM}\sum_{i,j}|U^{k+1}(i,j) - U^k(i,j)| \leq s,$$

where NM is the number of pixels.
Let us also note the *very high efficiency* of *Newton's method* (summarized by equation (34) of section 5.4.1) for solving the equation (31). On average, the numerical solution of equation (31) is computed in 5 iterations; our stopping criterion is $|t^{k+1} - t^k| \leq 10^{-20}$.

6.1 Experiments with synthetic images

We have tested our semi-implicit algorithm on several *synthetic images* provided by various types of surfaces. In such tests, we can compare the reconstructed surfaces with the groundtruth. In all the examples, the errors noted ϵ_1, ϵ_2 and ϵ_∞ are the mean absolute errors between the reference and reconstructed surfaces measured according to the L_1, L_2 and L_∞ norms, respectively. They are measured with the logarithm of the depth modulation in the coordinate system of the camera, i.e. the approximations of the solution v of equation (13). Let us remind that the parameter f corresponds to the focal length.

6.1.1 Experiments on various synthetic images

In this first series of results, we show the original object (i.e. the groundtruth) from two points of view (in a) and b)), the input image obtained from the original object (in c)), the reconstructed surface from the same two points of view as the original object (in d) and e)). In f), we display the superposition of the reconstructed surface and the original object in the same point of view as e) . The groundtruth is always displayed in blue and the color of the reconstructed solution is gold (this holds for all the experiments with synthetic images). Let us recall that one of the most significant improvements of our method is that it can recover surfaces containing *several local mimima* (and maxima) *without any additional data*[30].

We have first tested our algorithm with images synthetized from such surfaces: in particular the "hills surface" diplayed in Figure 8-ab) and the field of bumps displayed in figure 9-ab). The second rows of these figures show the surfaces returned by our algorithm (starting from the supersolution v_0) after convergence. The results are visually excellent and the computed errors $\epsilon_1, \epsilon_2, \epsilon_\infty$ are very small. Let us emphasize that these solutions have been computed without *any boundary data* and that in this case, *none of the classical propagation/PDE's methods* ([27, 56, 16, 31, 30, 51, 52] among others can return a satisfying solution. At this stage, let us remind the reader that to be able to recover the original surface, this surface must verify the state constraints (described in section 4.2, page 12) on the boundary of the image. The hills surface and the field of bumps verify this constraint. In particular, the example of the hills surface shows how weak this constraint is. The classical Mozart's face associated to the paper by Zhang et al. [66] (Computer Vision Lab. of the university of Central Florida) is today an unavoidable test. We have also applied our algorithm to this surface, see Figure 10. In [52] we needed to fix the height of the singular point on the nose for obtaining a relatively satisfying solution. Here we do not need this information. Note that the reconstruction errors of Mozart's face are mainly located in the part of the image corresponding to the background of the scene. These errors are due to the large discontinuity of the groundtruth along the apparent contours of the face. Indeed, since we compute some

[30] We only use the image.

approximations of the viscosity solution which is continuous (due to the strong uniqueness), we are not able to recover discontinuous surfaces. Let us note that the theory we have developped assumes that the intensity image is *continuous*. Also, the surfaces and the images of Figure 8 and Figure 9 are continuous and smooth.

Nevertheless in order to test the ability of our algorithm to deal with discontinuous images we have applied it to synthetic images generated by shapes containing edges. First, we use a surface containing (decreasing and increasing) edges such that all its maxima[31] are smooth, see Figure 11. In this case, the reconstruction is perfect. Second, we use a more complex surface containing (decreasing and increasing) edges with nonsmooth (local and global) maxima[31], see Figure 12. In this second case, the reconstructed surface is satisfying but not perfect. The size of the images of the hills, of the field of bumps, of the Mozart's face and of surfaces containing edges are respectively: 300×300, 400×400, 250×250, 250×250, 250×250.

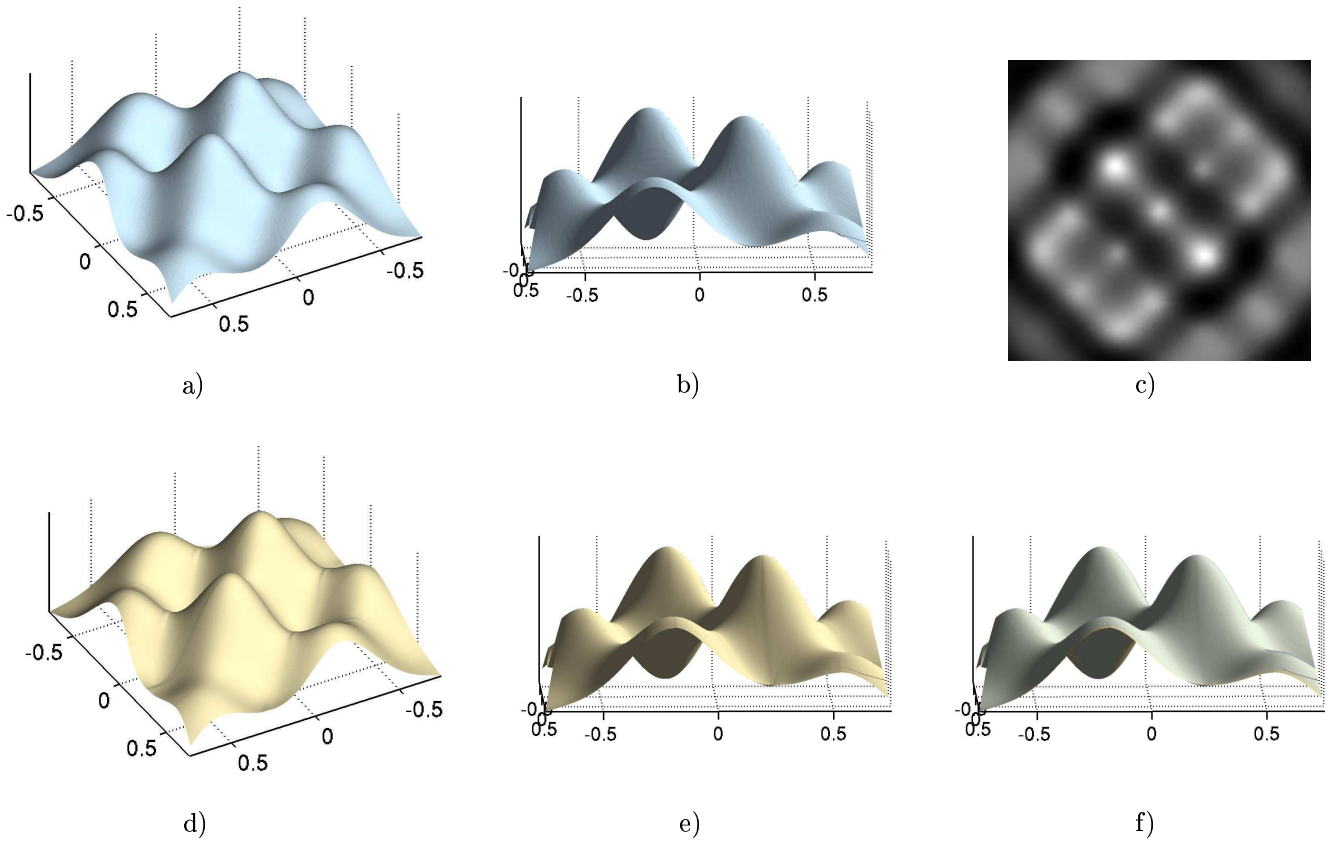

a) and b) original surface (groundtruth);
c) image obtained from the original surface a): $f = 20mm$, size$= 300 \times 300$;
d) and e) surface reconstructed from the image c): $n \simeq 65$, $\epsilon_1 \simeq 0.00152397$, $\epsilon_2 \simeq 0.0019405$, $\epsilon_\infty \simeq 0.00655214$;
f) superposition of the original surface (groundtruth) with the reconstructed surface (displayed in d) and e)).

Figure 8: Example of results for an image of a surface with several local minima: the "hill surface".

6.1.2 Robustness of our method

The second part of the experiments is aimed at demonstrating the robustness of our method to various errors on the parameters. For these tests, we have used only Mozart's face image.
In the series of figures associated to these experiments (Figures 16, 17, 18, 19, 20), we show:

[31] More precisely, we should consider the local *minima of the depth modulation*. The minima of depth modulation are approximately the maxima of the visualized surface.

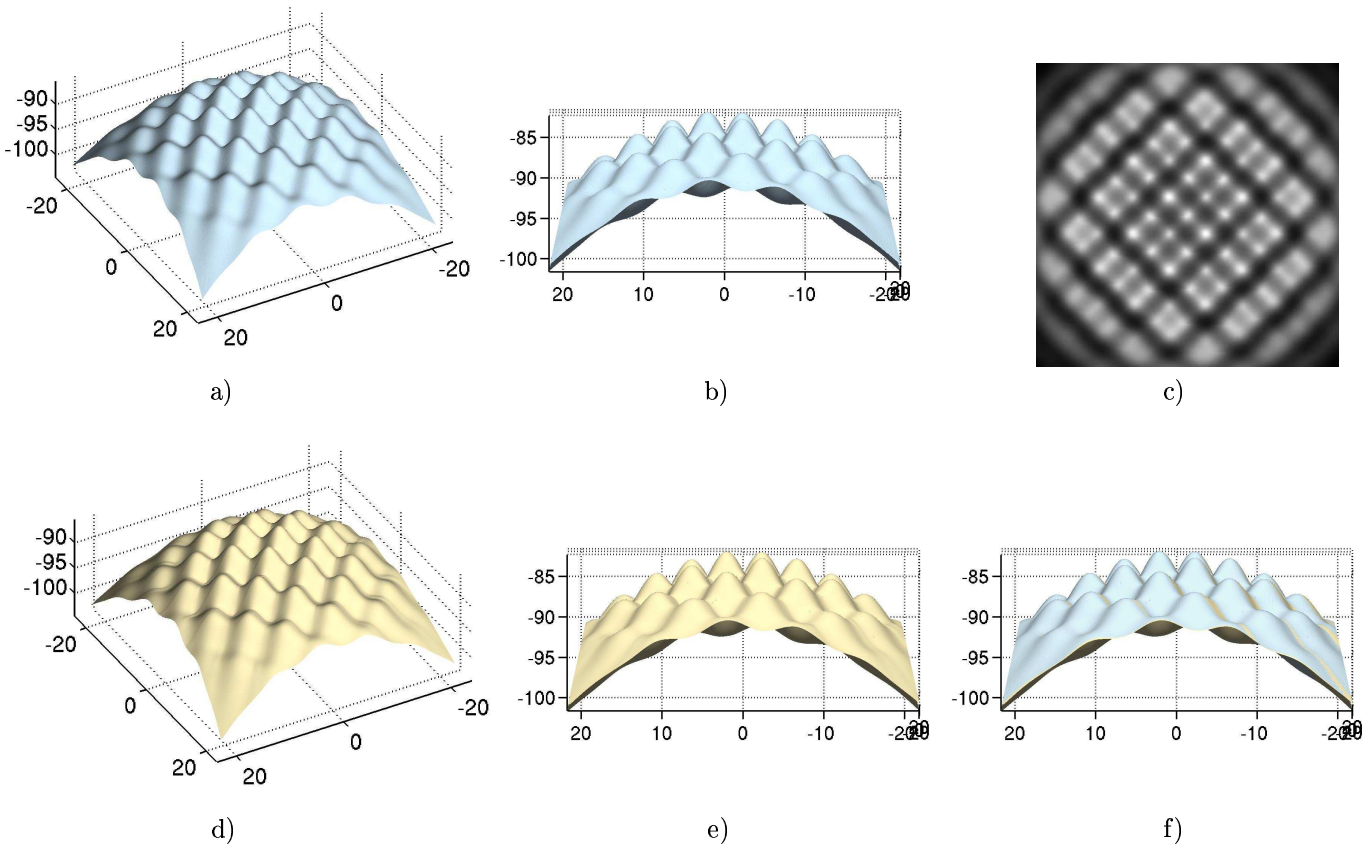

a) and b) original surface (groundtruth);
c) image obtained from the original surface a): $f = 23mm$, size= 400×400;
d) and e) surface reconstructed from the image c): $n \simeq 70, \epsilon_1 \simeq 0.00136196, \epsilon_2 \simeq 0.00170217, \epsilon_\infty \simeq 0.00579273$;
f) superposition of the original surface (groundtruth) with the reconstructed surface (displayed in d) and e)).

Figure 9: Example of results for the "field of bumps" image.

iteration (n)	ϵ_1 error	ϵ_2 error	ϵ_∞ error
0	3.58725	3.58753	3.68509
60	0.554503	0.558744	0.8996
120	0.205832	0.218589	0.683311
180	0.097647	0.111971	0.625567
240	0.0436155	0.0544579	0.593743
300	0.023504	0.029243	0.578646
360	0.0211661	0.0328685	0.576906
420	0.0213052	0.03496	0.576906
540	0.0213343	0.0350149	0.576906
600	0.0213343	0.0350149	0.576906
660	0.0213343	0.0350149	0.576906
720	0.0213343	0.0350149	0.576906

Table 1: Evolution of the errors associated to Figure 13: (Mozart's face) with the number of iterations, starting from the supersolution u_0.

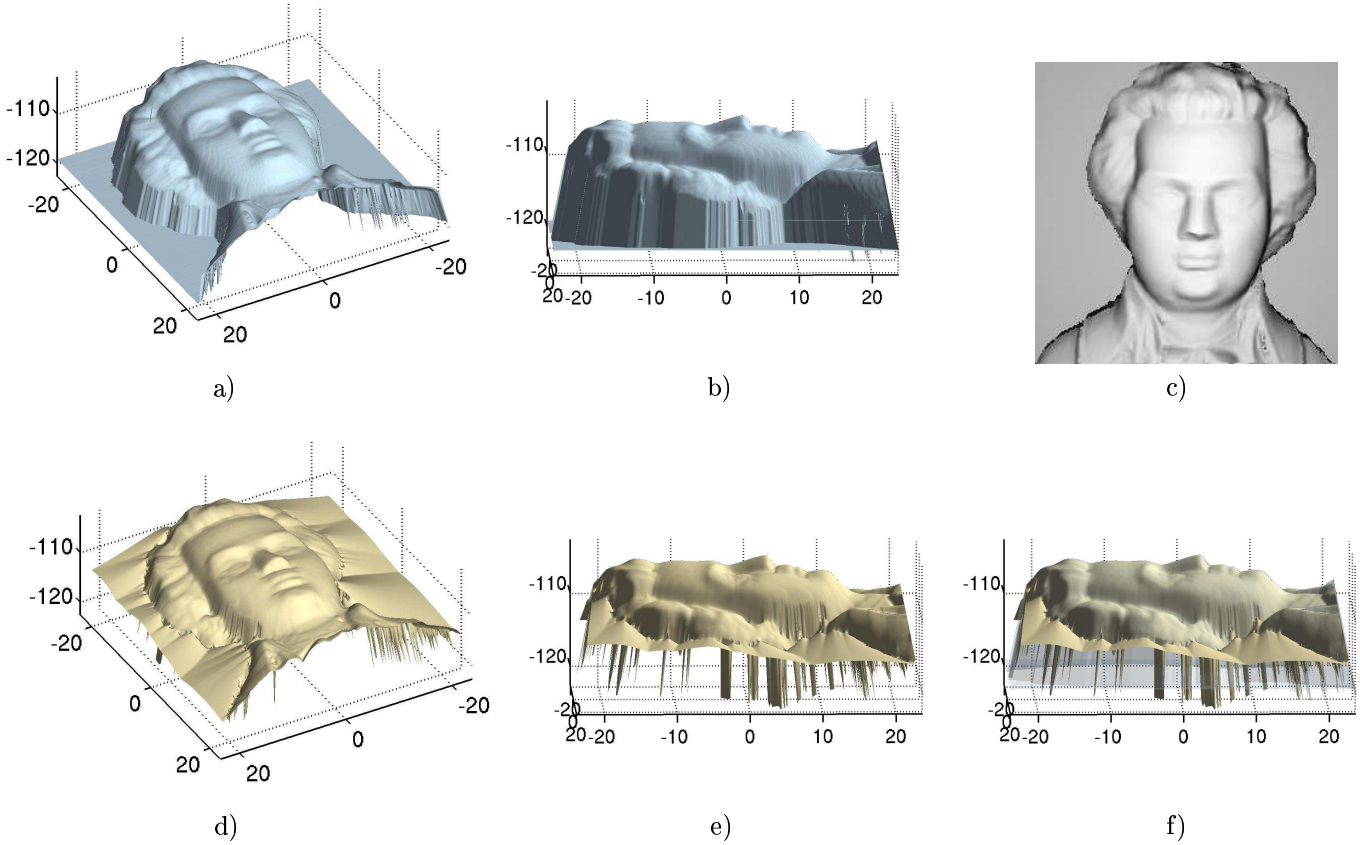

a) and b) original surface;
c) image obtained from the original surface a): $f = 25mm$, size= 250×250;
d) and e) surface reconstructed from the image c): $n \simeq 50$, $\epsilon_1 \simeq 0.0201287$, $\epsilon_2 \simeq 0.0332239$, $\epsilon_\infty \simeq 0.109705$;
f) superposition of the original surface (groundtruth) with the reconstructed surface (displayed in d) and e)).

Figure 10: Result for the image of Mozart's face.

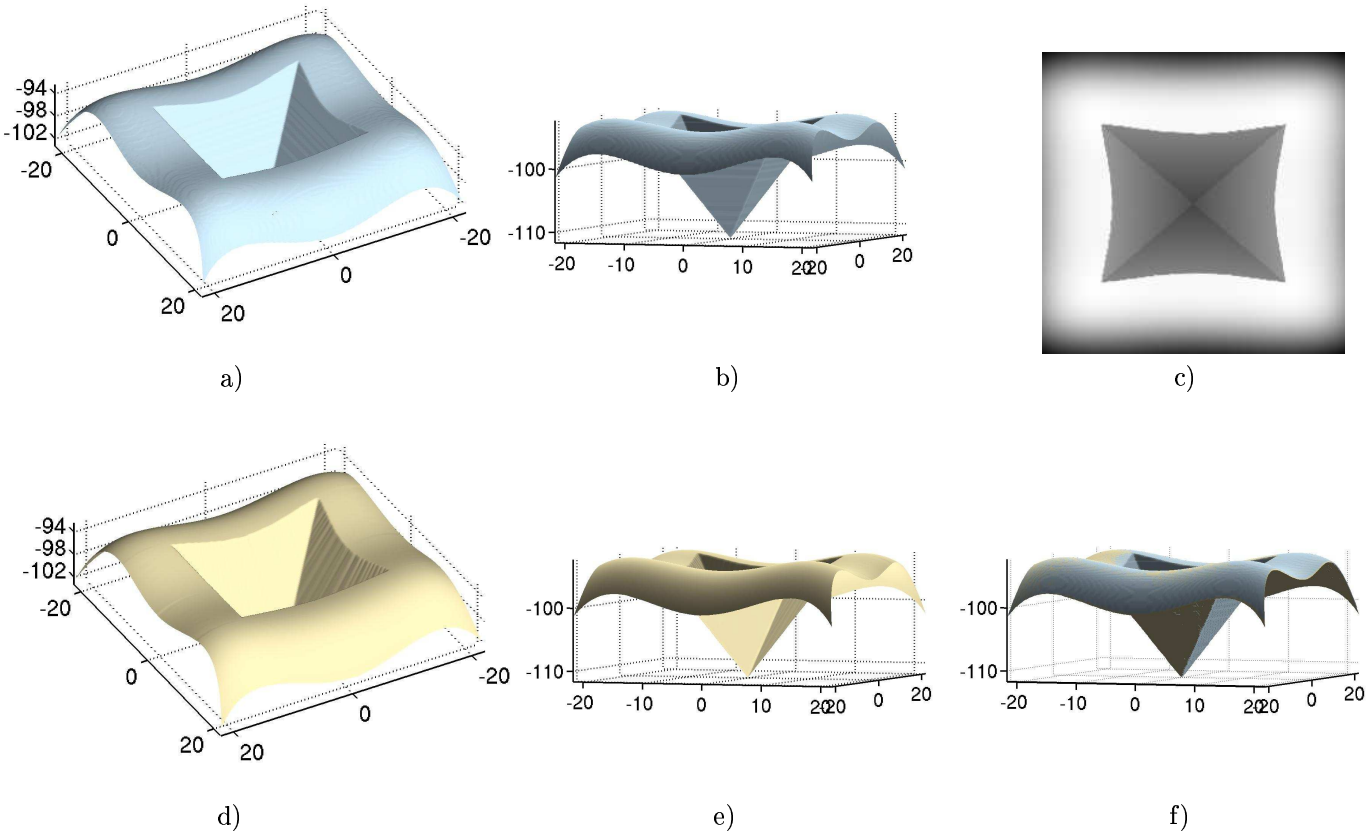

a) and b) original surface;
c) image obtained from the original surface a): $f = 23mm$, size= 250×250;
d) and e) surface reconstructed from the image c): $n \simeq 60$, $\epsilon_1 \simeq 0.00098814$, $\epsilon_2 \simeq 0.00139067$, $\epsilon_\infty \simeq 0.0094318$;
f) superposition of the original surface (groundtruth) with the reconstructed surface (displayed in d) and e)).

Figure 11: Result for an image containing discontinuities.

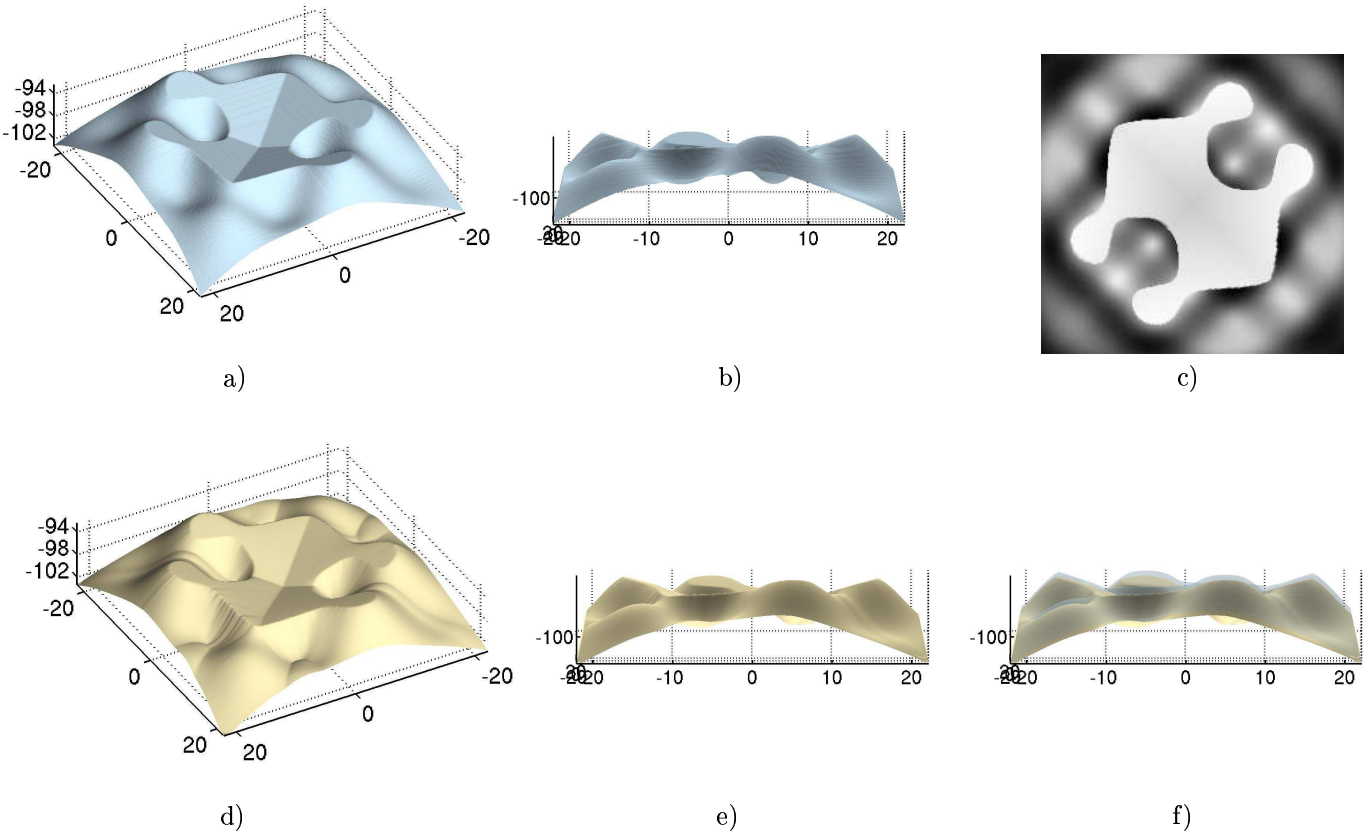

a) and b) original surface (groundtruth);
c) image obtained from the original surface a): $f = 23mm$, size= 250×250;
d) and e) surface reconstructed from the image c): $n \simeq 85$, $\epsilon_1 \simeq 0.00356152$, $\epsilon_2 \simeq 0.00407986$, $\epsilon_\infty \simeq 0.0265672$;
f) superposition of the original surface (groundtruth) with the reconstructed surface (displayed in d) and e)).

Figure 12: Results for another image containing discontinuities.

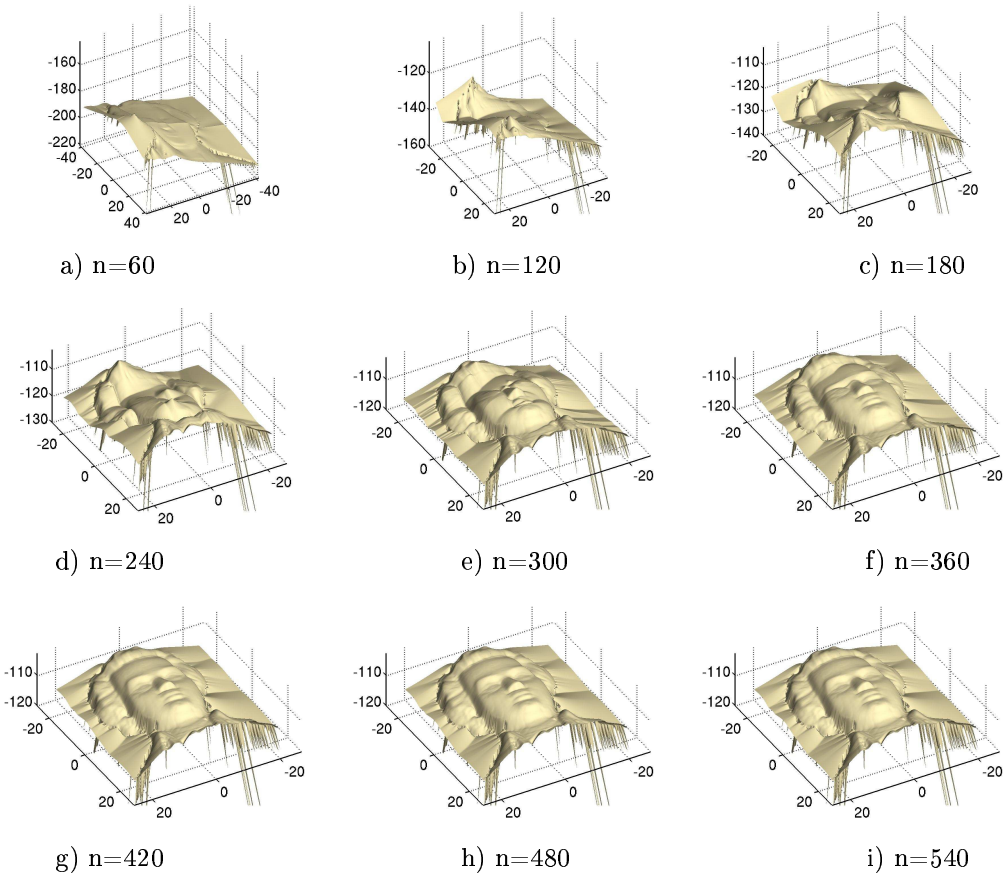

a) n=60 b) n=120 c) n=180

d) n=240 e) n=300 f) n=360

g) n=420 h) n=480 i) n=540

Figure 13: Evolution of the reconstructed surface for the image of Mozart's face, starting from the supersolution u_0 (for errors, see Table 1)

.

iteration (n)	ϵ_1 error	ϵ_2 error	ϵ_∞ error
0	0.0302943	0.0460551	0.180416
2	0.0220833	0.0312264	0.137289
4	0.0158622	0.0215666	0.124512
6	0.0133733	0.0177039	0.120779
10	0.0126053	0.0183098	0.111928
15	0.0133472	0.0213313	0.106305
20	0.0147987	0.0247051	0.108798
25	0.0165059	0.0277196	0.109686
30	0.0174543	0.0292335	0.109704
35	0.0185734	0.0309366	0.109705
40	0.0188836	0.0313961	0.109705
50	0.0201287	0.0332239	0.109705
60	0.0206475	0.0339851	0.109705
70	0.0208931	0.0343325	0.109705
80	0.0209713	0.0344363	0.109705

Table 2: Evolution of the errors associated to Figure 14: (Mozart's face) with the number of iterations, starting from the supersolution v_0.

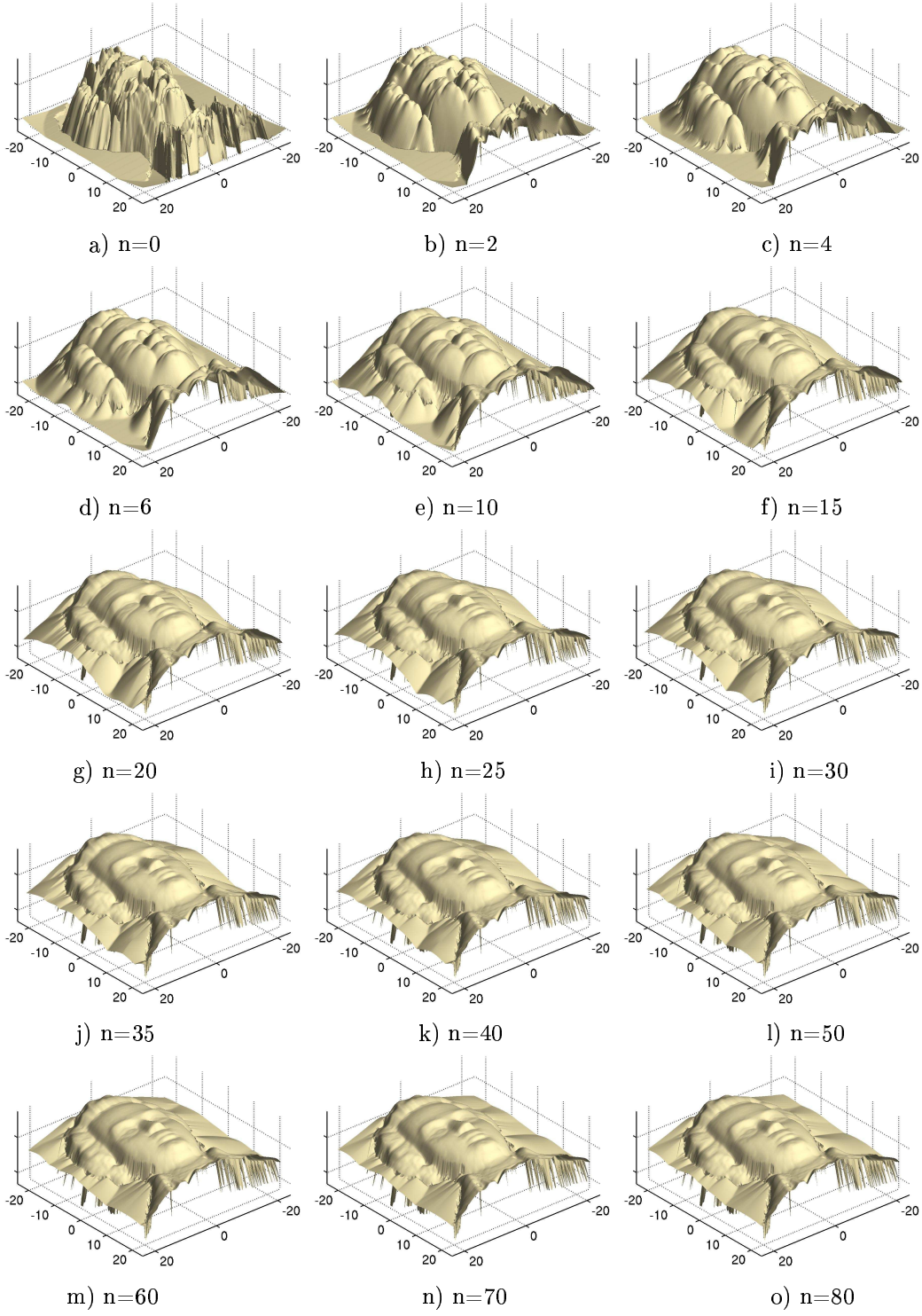

Figure 14: Evolution of the reconstructed surface for the image of Mozart's face, starting from the supersolution v_0 (for errors, see Table 2).

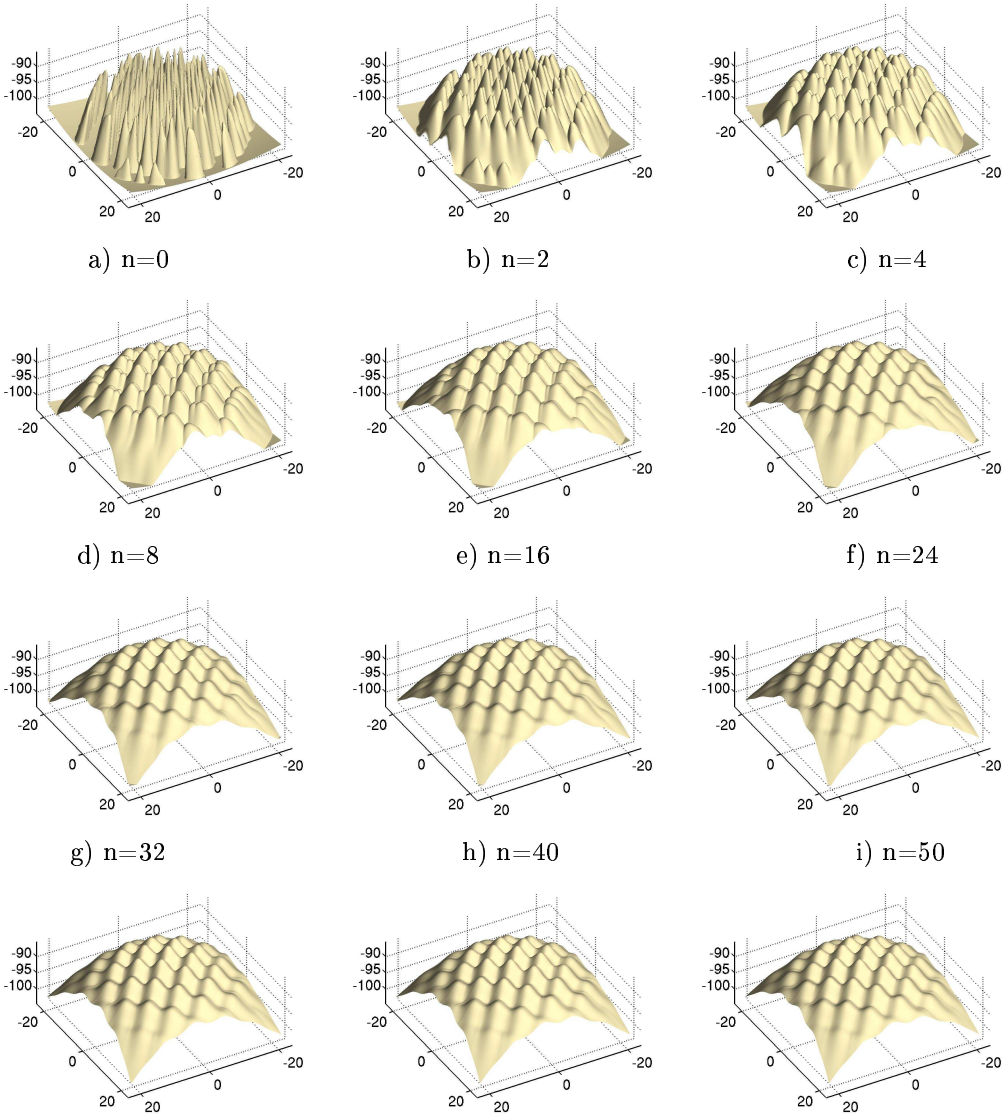

a) n=0 b) n=2 c) n=4

d) n=8 e) n=16 f) n=24

g) n=32 h) n=40 i) n=50

j) n=60 k) n=70 l) n=80

Figure 15: Evolution of the reconstructed surface from the image of the "field of bumps", starting from the supersolution v_0 (for errors, see Table 3).

iteration (n)	ϵ_1 error	ϵ_2 error	ϵ_∞ error
0	0.00134159	0.00167079	0.00474082
2	0.042826	0.0488785	0.117484
4	0.0276274	0.033543	0.10354
8	0.0147751	0.0197772	0.0751836
16	0.00667883	0.0105963	0.0485785
24	0.0039321	0.00657979	0.0332412
32	0.00273465	0.00440412	0.0225997
40	0.00205176	0.00310148	0.0152853
50	0.00160707	0.00222596	0.0116531
60	0.00142766	0.00183524	0.00877063
70	0.00136196	0.00170217	0.00579273
80	0.00134347	0.00167312	0.00474082
90	0.00134163	0.00167086	0.00474082
100	0.00134159	0.00167079	0.00474082

Table 3: Evolution of the errors associated to Figure 15: ("field of bumps") with the number of iterations, starting from the supersolution v_0.

- in the first row, the reconstruction obtained without noise and with the exact input parameters, as a reference;
- in the other rows, some reconstructions obtained with corrupted images and/or with errors on some parameters;
- in the first column, the input images when they have been corrupted;
- in the second and third column, the reconstructed surfaces from two points of view.
- in the last column, the superpositions of the reconstructed surface with the groundtruth.

We show the stability of our method with respect to five types of errors:

1. *image intensity errors due to noise.* Uniformly distributed white noise has been added to all pixels of the input images and the corresponding reconstructed surfaces are shown, see Figure 16. The Signal to Noise Ratio (SNR) is equal to 10.63, 5.32 and 2.65 in images Fig.16-e), Fig.16-i), and Fig.16-m), respectively. As seen from this figure, our algorithm is quite robust to intensity noise.

2. *gamma factor.* Most of the usual image acquisition devices do not have a linear intensity response. The actual response is usually well approximated by a power law, whose exponent is the gamma factor. If $\gamma = 1$ the response is linear. Typical values of γ range between 0.5 and 2.5. Figure 17 shows the reconstruction results when the algorithm is run on the original image raised to the power 0.5 and 2. The result corresponding to $\gamma = 0.5$ is flatter than the real surface whereas the form of the surface reconstructed with $\gamma = 2$ if amplified. Let us note that even if quantitavely the numerical errors are important (due to the global and large deformation of the surface), these results are qualitatively very good.

3. *errors made on the parameters of the imaging system*, on the *calibration of the intensity of the light source* and on the *albedo* of the surface. As explained in section 2, these parameters are contained in the constant coefficient σ_2 of equation (6)

$$E_i = \sigma_2 \frac{\cos\theta_i}{r^2}.$$

Thus, for simulating errors on these parameters we distort the image by a linear transformation.
From the theoretical point of view, if we make an error on the σ_2 parameter, the input image is therefore

$I_\lambda = \lambda I$ instead of I (where $\lambda = \frac{\sigma_2}{\sigma_\epsilon} > 0$ and where σ_ϵ is the distorted parameter). Also, the algorithms compute some approximations of the solution of equation

$$-u(x)^{-2} + I_\lambda(x) f^2 \frac{\sqrt{[f^2|\nabla u(x)|^2 + (\nabla u(x)\cdot x)^2]/Q(x)^2 + u(x)^2}}{u(x)} = 0 \tag{36}$$

instead of equation (12).
Let u the viscosity solution of (12) (with state constraints). Clearly, u is the solution of equation (with state constraints)

$$-\lambda u(x)^{-2} + \lambda I f^2 \frac{\sqrt{[f^2|\frac{\nabla u(x)}{\sqrt{\lambda}}|^2 + (\frac{\nabla u(x)}{\sqrt{\lambda}}\cdot x)^2]/Q(x)^2 + \left(\frac{u(x)}{\sqrt{\lambda}}\right)^2}}{\frac{u(x)}{\sqrt{\lambda}}} = 0;$$

so it is the solution of equation (with state constraints)

$$-\left(\frac{u(x)}{\sqrt{\lambda}}\right)^{-2} + I_\lambda f^2 \frac{\sqrt{[f^2|\frac{\nabla u(x)}{\sqrt{\lambda}}|^2 + (\frac{\nabla u(x)}{\sqrt{\lambda}}\cdot x)^2]/Q(x)^2 + \left(\frac{u(x)}{\sqrt{\lambda}}\right)^2}}{\frac{u(x)}{\sqrt{\lambda}}} = 0.$$

By change of unknown, $u_\lambda = \frac{u(x)}{\sqrt{\lambda}}$ is the viscosity solution of equation[32] (36). In other words, errors on the σ_2 parameter just involve changes of scale.
In practice, the experiments confirm this theoretical remark. Figure 18 shows two examples of reconstructions with such distortions. The intensities I_λ of the images Fig.18-e) and Fig.18-i) correspond to $1.2I$ and $0.8I$, where I is the intensity of the original image Fig.18-a). Of course, due to these changes of scale, the absolute errors ϵ_1, ϵ_2, ϵ_∞ are important, but the shapes of the reconstructed faces are satisfactory.

4. *incorrect estimation of the focal length* f of the camera. We show in Figure 19 that errors of $10mm$ (40%) on the focal length parameter f do not affect much the reconstructed surface. The image used in these experiments is the image Fig.10-c). The focal length used for synthetizing this image is $f = 25mm$. The last two rows of Figure 19, show the reconstructions for $f_\epsilon = 15mm$ and $f_\epsilon = 35mm$.

5. *modeling errors.* In practice with real images, the *light source is never located exactly at the optical center.* For example when we use a camera equipped with a flash (situation corresponding quite nicely to the modeling hypotheses), the light source is generally located at several centimeters from the optical center. Note nevertheless that the distance between the flash and the optical center is usually inferior to $10cm$. For testing the robustness of our method to this kind of errors, we have synthetized a series of images of Mozart's face with the light source located at $10cm$ and $20cm$, above, under, to the right and to the left of the optical center, see Figure 21. In Figures 22 and 23, we show the reconstructions obtained from these images. In Fig.22 we display the reconstructed surfaces from a frontal point of view; in Fig.23 we display the same surfaces from the side. As the reader can see, in all cases, the reconstructed surfaces are very good when the the light source is located at 10 cm. When the light source is located at 20 cm, the distortions are more important, but the results are still quite good. In Figures 21, 22 and 23 $\mathbf{P}_L$ is the position of the light source in the coordinate system of the scene. Let us recall that the optical center is located at $O = (0,0,0)$.

In Figure 20, we display the results for some images of Mozart's face corrupted by *pixel noise*, *gamma corrections*, *albedo errors*, and obtained with the *wrong focal length* f. In addition to the accumulation effect, let us note that the errors imposed are quite important. Surprisingly, the algorithm produces relatively satisfying results given the large difference between the original image and the input images.

6.2 Experimental results on real images

In this section we show some examples of reconstructions with *real images.* We have constructed a small database of real images of faces verifying approximately our modeling assumptions. A sample of this database is shown in Figure 28. This database is available online from:

[32] With state constraints.

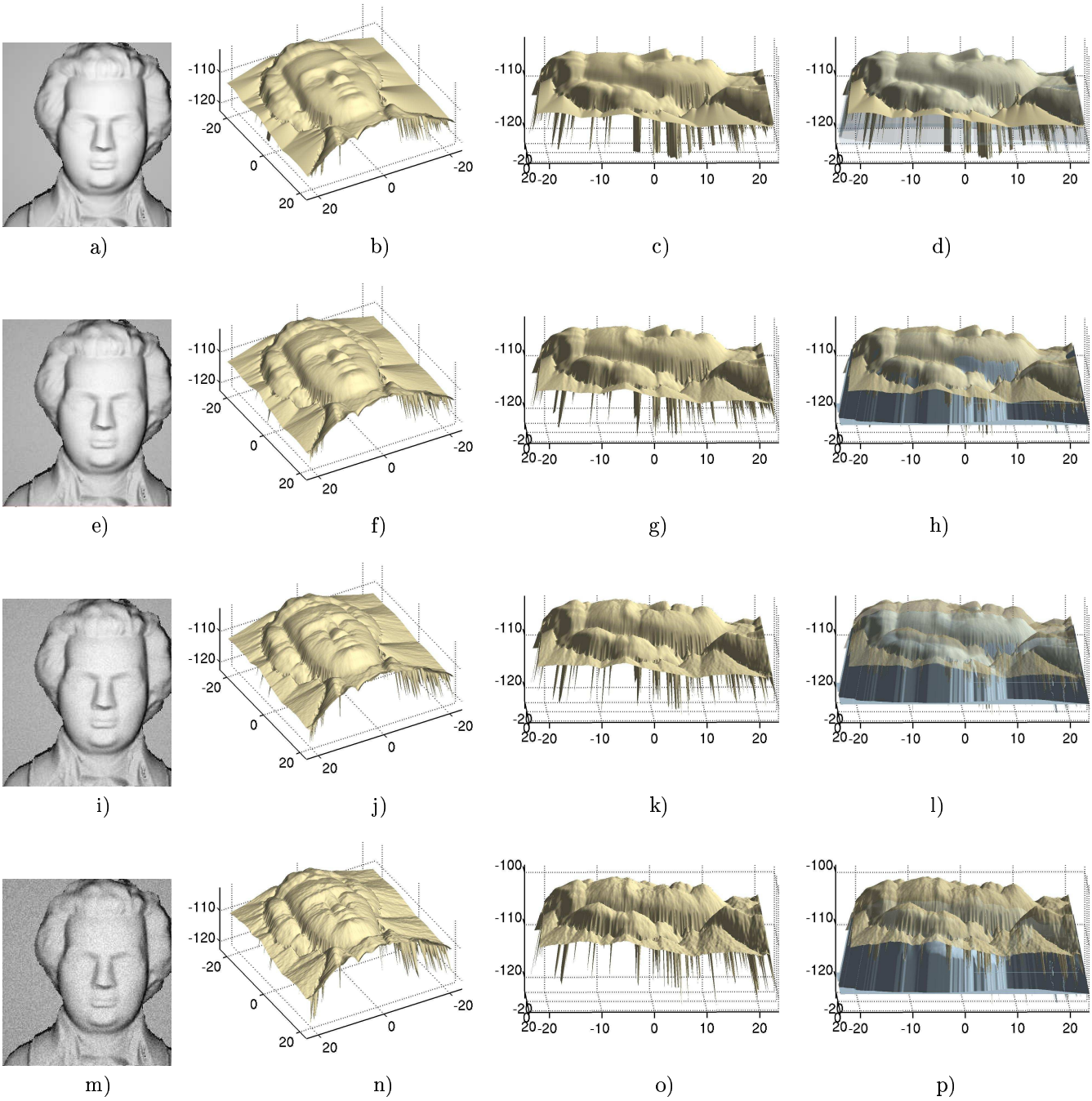

a) original image; b) and c) surface reconstructed from image a);
e) noisy image with a $SNR = 10.63$; f) and g) surface reconstructed from image e);
i) noisy image with a $SNR = 5.32$; j) and k) surface reconstructed from image i);
m) noisy image with a $SNR = 2.65$; n) and o) surface reconstructed from image m);
In the last column, we display the superpositions of the reconstructed surfaces with the groundtruth.
For errors, see Table 4.

Figure 16: Results for the noisy images of Mozart's face.

image	noise/SNR	iteration	ϵ_1 error	ϵ_2 error	ϵ_∞ error
Fig.16-e)	10.63	$\simeq 50$	0.0266365	0.0386745	0.574023
Fig.16-i)	5.32	$\simeq 50$	0.0358871	0.0450536	0.569604
Fig.16-m)	2.65	$\simeq 50$	0.0554078	0.0612147	0.560532

Table 4: Errors associated to Figure 16 for the noisy images of Mozart's face.

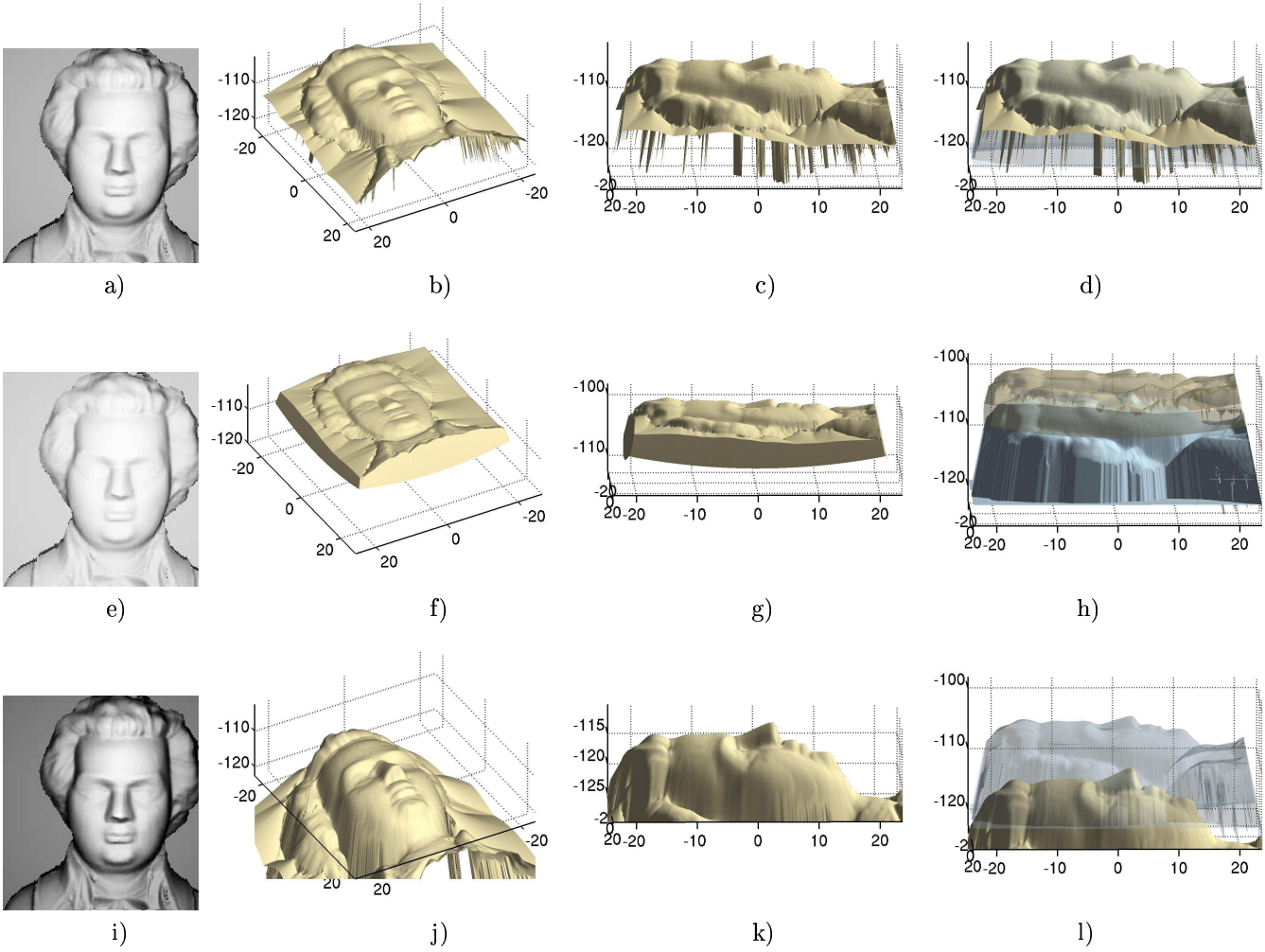

a) original image; b) and c) surface reconstructed from image a);
e) image distorted with $\gamma = 0.5$ ($I_\epsilon = \sqrt{I}$);
f) and g) surface reconstructed from image e): $n \simeq 45$, $\epsilon_1 \simeq 0.0559719$, $\epsilon_2 \simeq 0.0568014$, $\epsilon_\infty \simeq 0.079711$;
i) image distorted with $\gamma = 2$ ($I_\epsilon = I^2$);
j) and k) surface reconstructed from image i): $n \simeq 50$, $\epsilon_1 \simeq 0.126682$, $\epsilon_2 \simeq 0.146416$, $\epsilon_\infty \simeq 3.60861$;
In the last column, we display the superpositions of the reconstructed surfaces with the groundtruth.

Figure 17: Results for the images of Mozart face distorted by *gamma distortions* $\gamma = 0.5$ and $\gamma = 2$, i.e. instead of the real image I we used $\sqrt{I}$ and I^2.

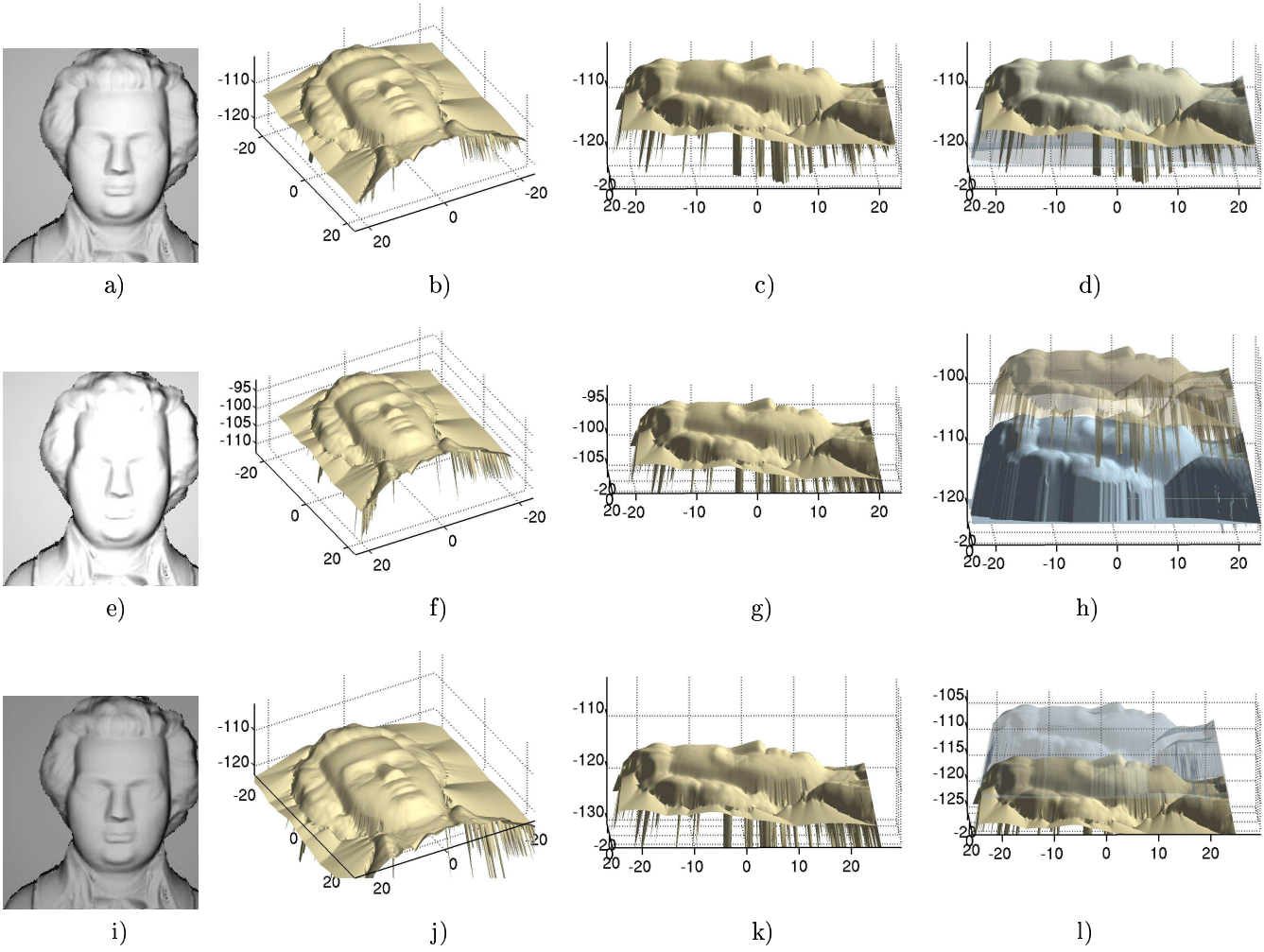

a) original image; b) and c) surface reconstructed from image a) with the correct constant coefficient σ;
e) distorted image $I_\epsilon = 1.2I$; f) and g) surface reconstructed from image e);
$n \simeq 40$, $\epsilon_1 \simeq 0.0719292$, $\epsilon_2 \simeq 0.077584$, $\epsilon_\infty \simeq 0.668079$;
i) distorted image $I_\epsilon = 0.8I$; j) and k) surface reconstructed from image i);
$n \simeq 50$, $\epsilon_1 \simeq 0.130974$, $\epsilon_2 \simeq 0.134119$, $\epsilon_\infty \simeq 0.46533$;
In the last column, we display the superpositions of the reconstructed surfaces with the groundtruth.

Figure 18: Results for the images of Mozart's face distorted by some *intensity scaling* corresponding to a *distortion of the constant coefficient* σ (this contains the *albedo* distortion).

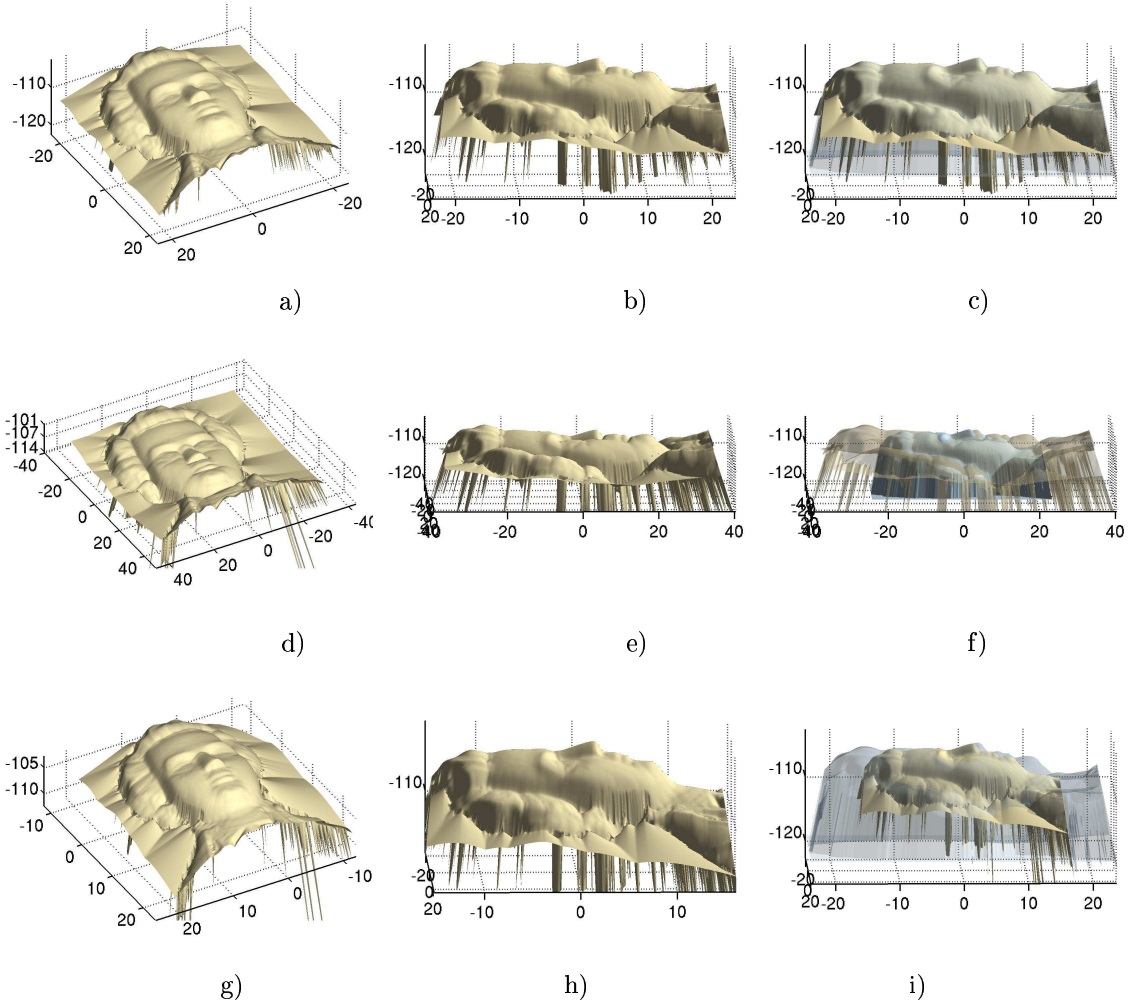

a) and b) surface reconstructed from image Fig.10-c) with the correct focal length parameter $f = 25mm$;
$n \simeq 54$, $\epsilon_1 \simeq 0.0213$, $\epsilon_2 \simeq 0.0350$, $\epsilon_\infty \simeq 0.577$;
c) and d) surface reconstructed from image Fig.10-c) with the distorted focal length parameter $f_\epsilon = 15mm$;
$n \simeq 45$, $\epsilon_1 \simeq 0.507348$, $\epsilon_2 \simeq 0.507873$, $\epsilon_\infty \simeq 1.22922$;
e) and f) surface reconstructed from image Fig.10-c) with the distorted focal length parameter $f_\epsilon = 35mm$;
$n \simeq 60$, $\epsilon_1 \simeq 0.369157$, $\epsilon_2 \simeq 0.370821$, $\epsilon_\infty \simeq 0.457924$;
In the last column, we display the superposition of the reconstructed surface with the groundtruth.

Figure 19: Results obtained from Mozart's face image with *distorted focal length parameter* f.

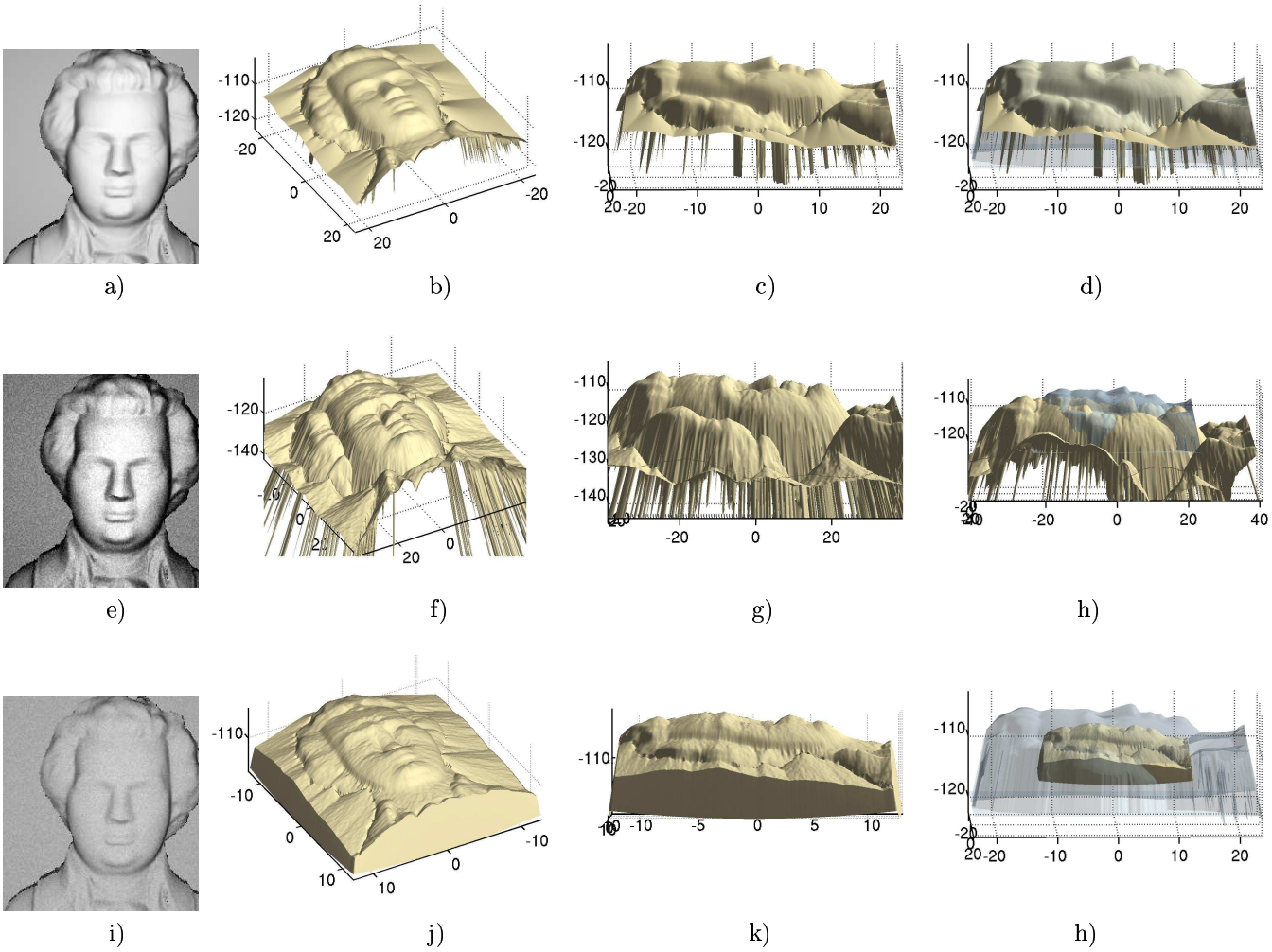

a) original image; b) to d) surface reconstructed from image a) with all the correct parameters;
e) image a) distorted by noise with a SNR equal to 4.04, by a gamma distortion $\gamma = 2$ and by an albedo distortion $\sigma_\epsilon = 1.2\sigma$;
f) to h) surface reconstructed from image e) with a wrong focal length parameter $f_\epsilon = 15mm$ (the correct parameter is $f = 25mm$): $n \simeq 40$, $\epsilon_1 \simeq 0.610511$, $\epsilon_2 \simeq 0.61432$, $\epsilon_\infty \simeq 4.2899$;
i) image a) corrupted by noise with a SNR equal to 3.36, by a gamma distortion $\gamma = 0.5$ and by an albedo distortion $\sigma_\epsilon = 0.8\sigma$;
j) to l) surface reconstructed from image i) with a wrong focal length parameter $f_\epsilon = 45mm$: $n \simeq 50$, $\epsilon_1 \simeq 0.5105$, $\epsilon_2 \simeq 0.5432$, $\epsilon_\infty \simeq 2.2899$.
In the last column, we display the superpositions of the reconstructed surfaces with the groundtruth.

Figure 20: Results for the image of Mozart's face distorted by *pixel noise*, by *gamma γ distortions*, by *albedo σ errors*, and with a *wrong focal length f*.

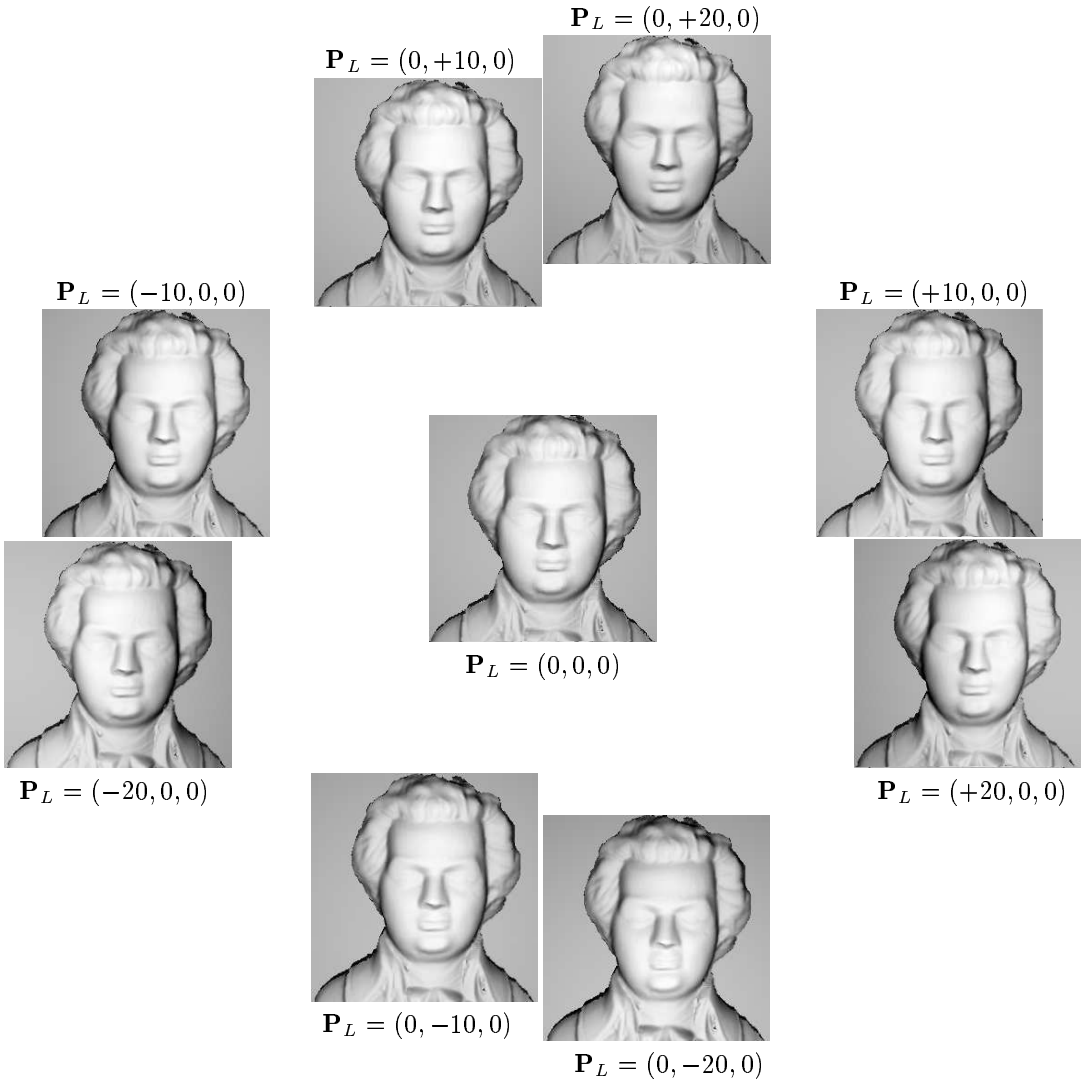

$\mathbf{P}_L$ is the position of the light source in the coordinate system of the scene. The optical center is located at $O = (0, 0, 0)$.

Figure 21: Images of Mozart's face with the light source located at $10cm$ or $20cm$, above, under, to the right or to the left of the optical center.

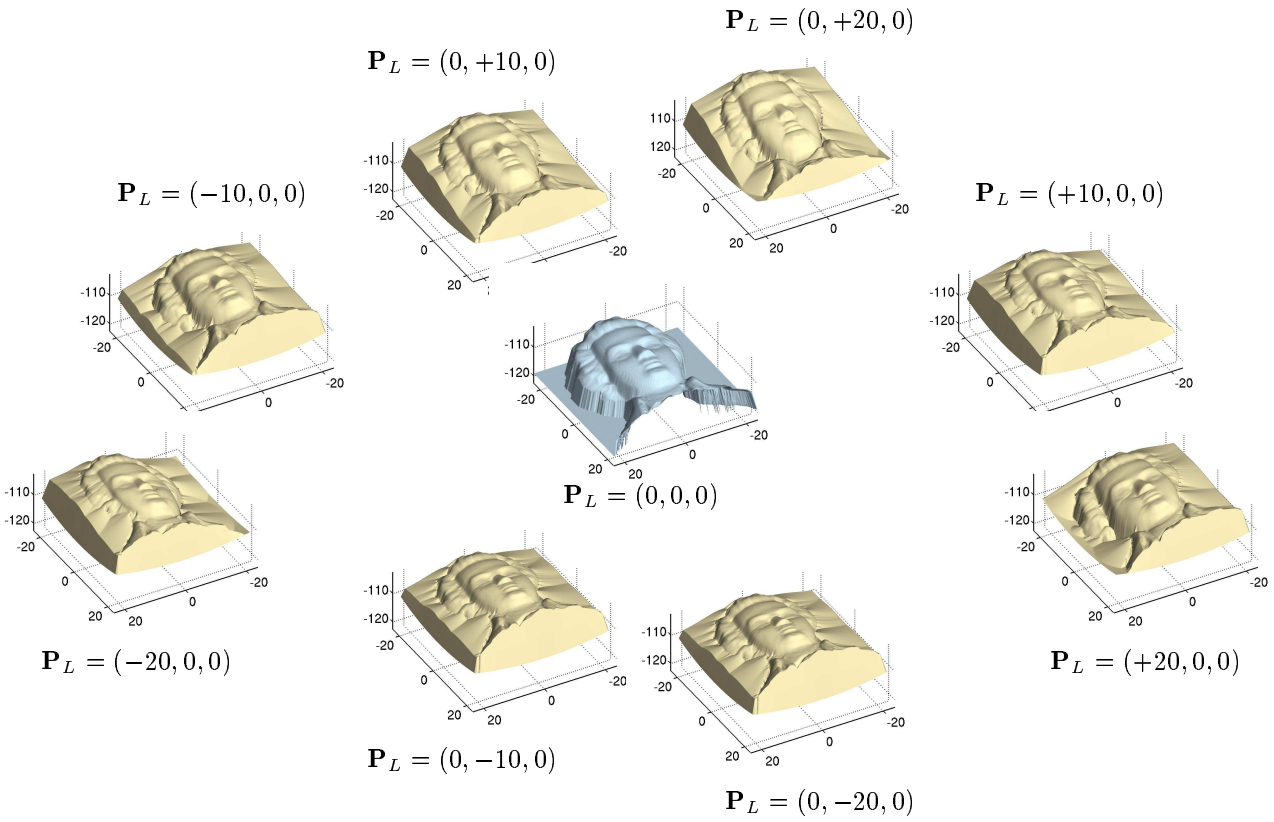

Figure 22: Reconstructed surfaces from the images of Mozart's face with the light source located at $10cm$ or $20cm$, above, under, to the right or to the left of the optical center; these images are displayed in figure 21.

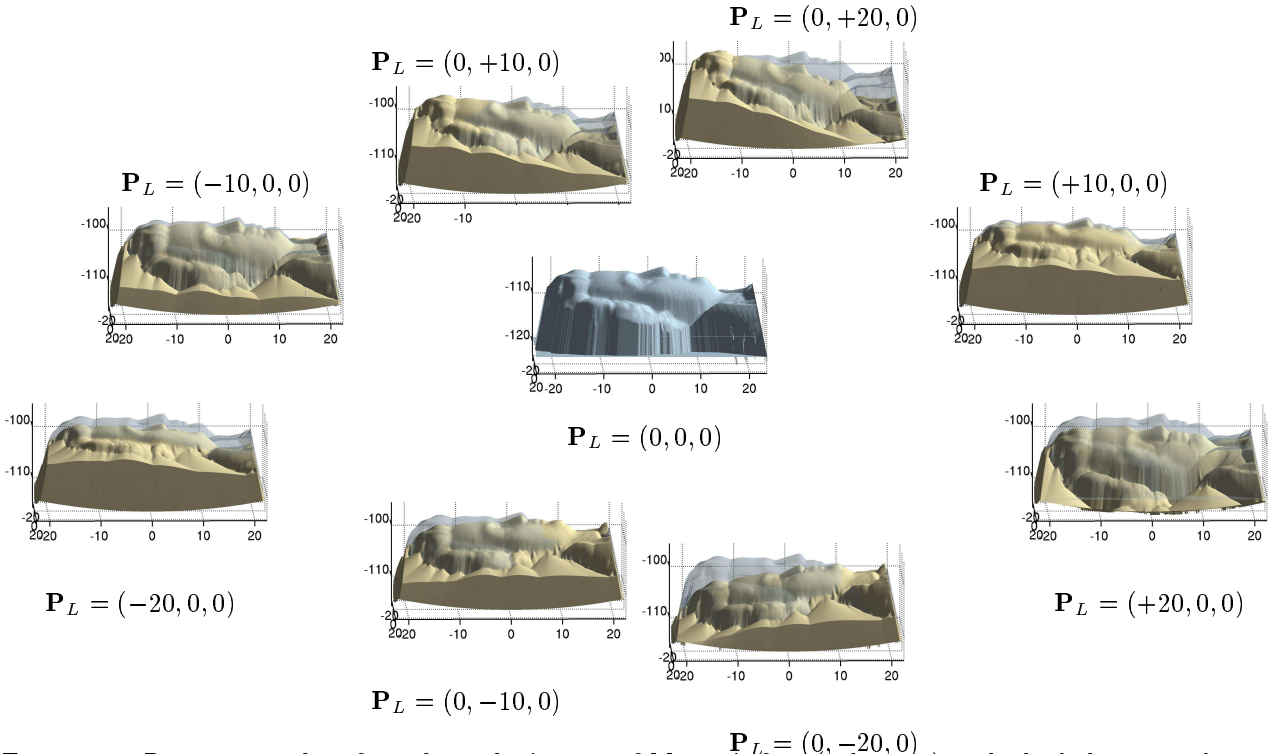

Figure 23: Reconstructed surfaces from the images of Mozart's face (side view) with the light source located at $10cm$ or $20cm$, above, under, to the right or to the left of the optical center; these images are displayed in figure 21.

`http://www-sop.inria.fr/odyssee/team/Emmanuel.Prados/index.en.html`

For generating this database, we have used the same cheap digital camera as for the experiments of [50] (the Pentax Optio 330GS). So the size of the pixels of the images provided by the camera is approximately $0.0045 \times 0.0045\ mm^2$ (CCD size = 1/2.7"). For reducing the pixel noise and the computation time, we have resized the images. The original images contain 2048×1536 pixels. The reduced images contain 512×384 pixels. After resizing, the size of the pixels is estimated to $0.018 \times 0.018\ mm^2$. For all these images, the focal length was fixed to 5.8 mm. The photos have been taken in an approximately dark place.

In our experiments, we need to fix the parameter σ_2 introduced in equation (6)

$$E_i = \sigma_2 \frac{\cos\theta_i}{r^2}$$

(see page 6). In these tests we have chosen to fix $\sigma_2 = 1000$. In the previous section, we have proved that a modification of the constant σ_2 involves a change of scale in the reconstruction. Figure 27 illustrates this. In this figure, to the right of each reconstructed surface, we show (in blue) the value of the σ_2 constant used. Note that the values on the axes of the figures are in centimeters. Contrary to [50, 47], we do not have modified the gamma parameter of the image (we have fixed $\gamma = 1$).

Our modeling of the problem assumes that the scene is lambertian and the albedo is constant. Here, these hypotheses do not hold. For example, the albedo of the eyes is not the same as the albedo of the skin. Moreover it is not constant. Since the iris is very dark, they do not cause difficulties (they only have local effects). At the opposite, the white parts of the eyes can produce important peaks in the reconstruction (mathematically, we see that the surface is pulled up by the pixels with high intensity). To remove this problem, we have painted manually[33] the eyes, see Figure 24, for an example of reconstructions from an image with or without eye inpainting. Figures 25 and 26 show the same surface as Figure 24-d) from various points of view and with two different illuminations. Figure 29 displays the reconstructed surfaces from the images of Figure 28 (after having inpainted eyes); the photos and the associated reconstructions are ordered the same way. To our knowledge, none of the other SFS methods is able to return such results as ours...

In many of the reconstructions, one can see the appearance of peaks on the lips and on the forehead. These peaks are due to the highlights (the surfaces are clearly not Lambertian): contrary to the methods presented in [50, 47], this one seems fairly sensitive to highlights. Note methods allowing to automatically remove the highlights are available in the literature, e.g. the work of Ragheb and Hancock [55] and that of Tan et al. [60] (We have not tested these methods). We have also noticed that our new method can be fairly sensitive to salt and pepper noise. More precisely to "salt pixels" (but not to "pepper pixels"). In order to decrease this effect, we have first reduced the size of the images ($2048 \times 1536 \longrightarrow 512 \times 384$ pixels) and processed it with a simple filter reducing the "salt" effects.
In spite of these small defects, the results are quite satisfying and, to our knowledge, much better than those obtained by any of the previous SFS methods.

Let us mention that for all the images of Figure 28, the number of iterations required for recovering the surfaces of Figure 29 is inferior to 80.

To close this section, let us emphasize again that contrary to the experiments of [50, 47] which were also performed on a real image of a face, we do not need to fix the height of the singular point[34] on the nose anymore. In [50, 47], we need to know the very important prior that the tip of the nose is the point of the surface which is the closest to the optical center of camera. In the experiments presented here, besides the intensity image, we do not use additional data except the intrinsic parameters of the camera (focal length and size of pixels) and photometric calibration (σ_2 constant).

[33] This step can done automatically for example by matching the image to a model image already segmented. An example of a matching method is the robust multi-modal and non-rigid technique proposed by Hermosillo and Faugeras in [23].

[34] Let us recall that at the opposite of the framework of [50, 47], in our new and more realistic framework, the notion of singular points does not have sense anymore.

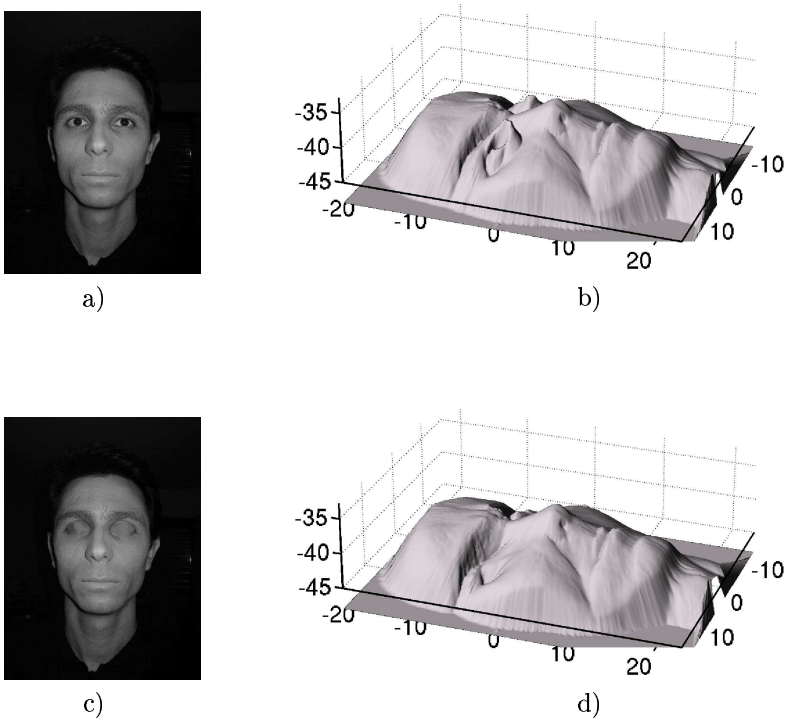

Figure 24: Example of reconstructions with or without eyes.

a) Original photo (512 × 384), b) surface reconstructed from a);
c) photo a) after we have painted the eyes, d) surface reconstructed from c).

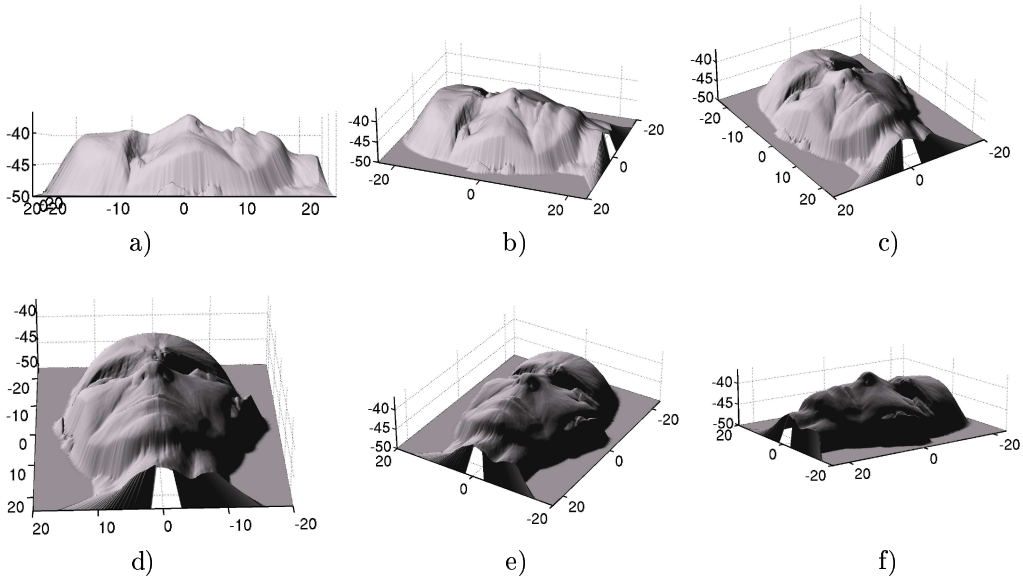

Figure 25: Surface reconstructed from the photo Fig.24-c) viewed from several points of view and illuminated by a single light source located at infinite. The light source direction is $(-49.00, 109, 100)$.

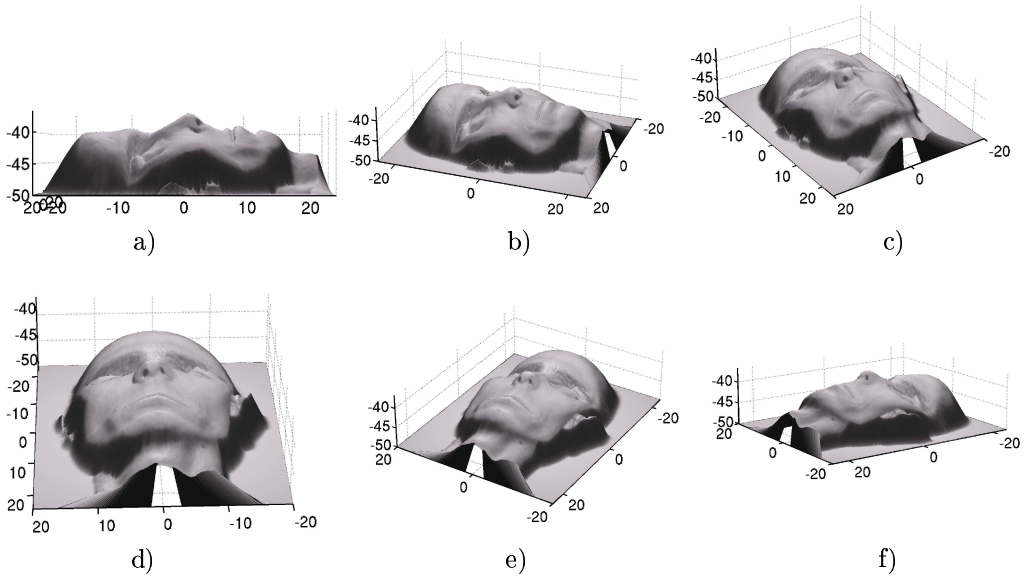

Figure 26: Same surface as Figure 25 illuminated by a single point light source located at the optical center, that is to say at (0,0,0).

7 Conclusion

The main difficulties encountered by the previous SFS work are due to the existence of singular points. Here, we have shown that these difficulties disappear completely when we model the SFS problem in a more realistic way than it is usually done. In effect, the notion of singular points does not make sense anymore when we do not neglect the $1/r^2$ attenuation term of the lighting. In other words, we have shown that in the previous SFS work, the problem is ill-posed because of an over-simplification in the modeling! Also, we have proved that generally in practice the SFS problem is well posed.
More precisely we have detailed the appropriate equations and Hamiltonians in the case where we do not neglect the $1/r^2$ lighting attenuation term, we have developed a **complete mathematical study** of the obtained equations (existence and uniqueness of the solution), we have designed schemes and algorithms allowing to approximate numerically the solution of our new PDE, we have proved the convergence of the computed approximations toward the solution, finally we have implemented and **tested with success** our new (semi-implicit) algorithm on synthetic images and **on real images**.

As predicted by the theory, in practice our method allows to **recover any surface** (which verifies hypothesis (18)) without any additional data or regularity assumptions. Let us stress the fact that our method works even when the surface has **several local minima** and maxima. There are not ambiguities anymore. To our knowledge none of the previous SFS methods is able to produce such results.

We are extending our approach for recovering non Lambertian surfaces.

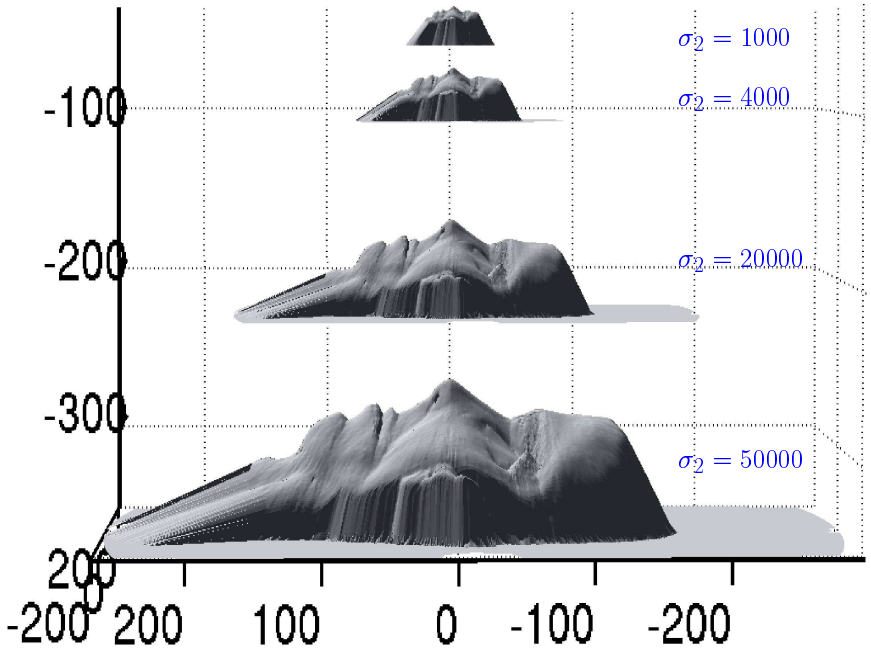

Figure 27: Influence of the errors on the σ_2 parameter (albedo of the surface).

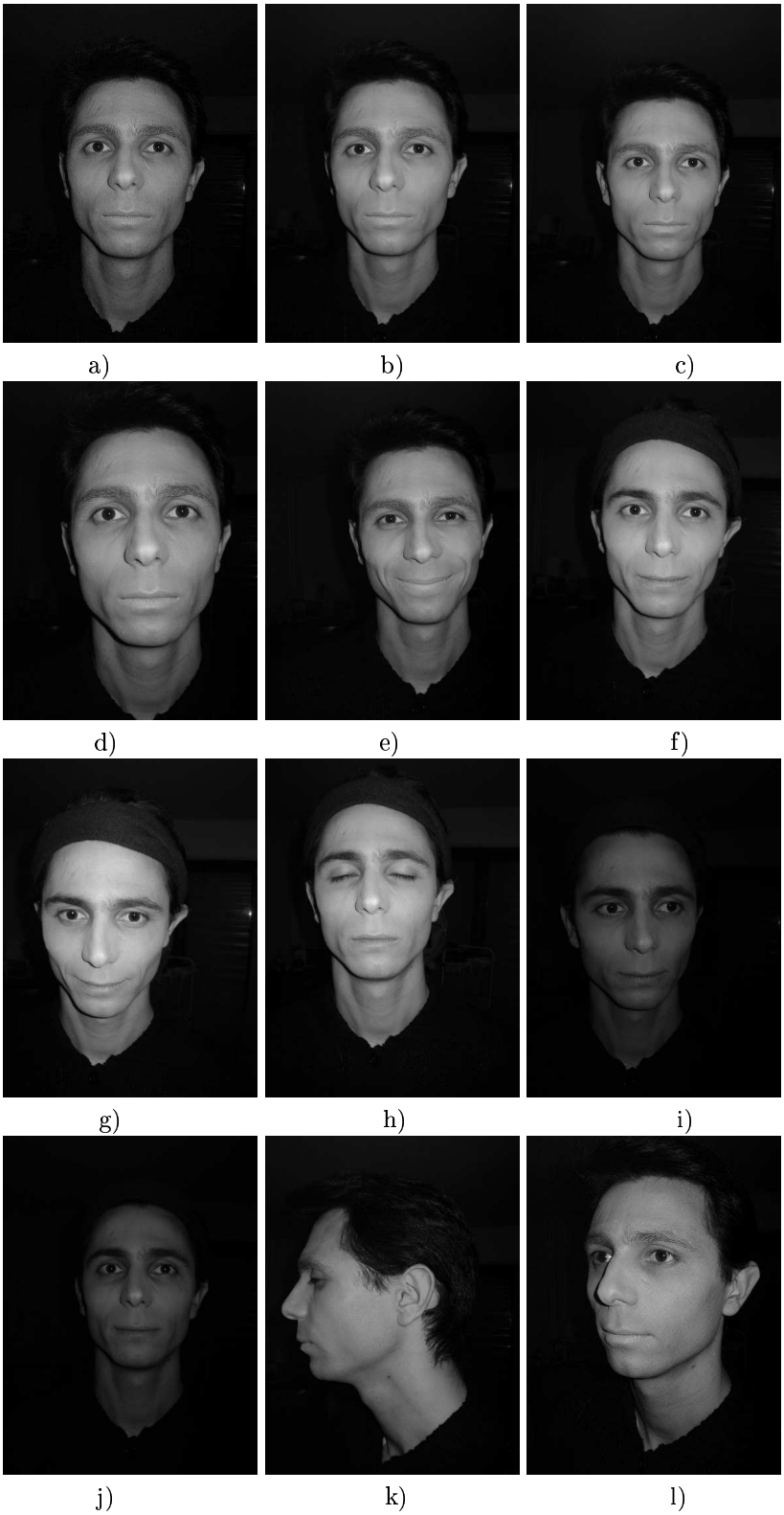

Figure 28: A sample of our database of real images of faces verifying approximately our modeling assumptions.

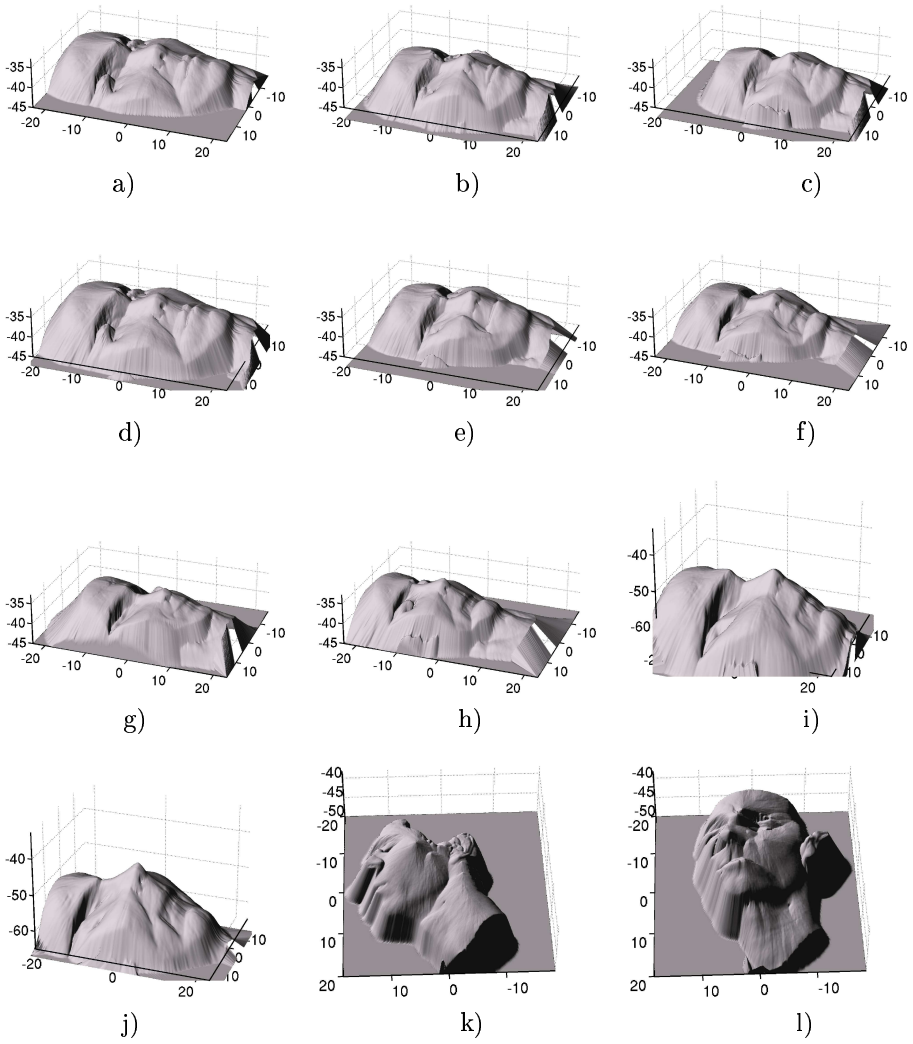

Figure 29: Surfaces reconstructed from the real images of Figure 28 (after having inpainted the eyes).

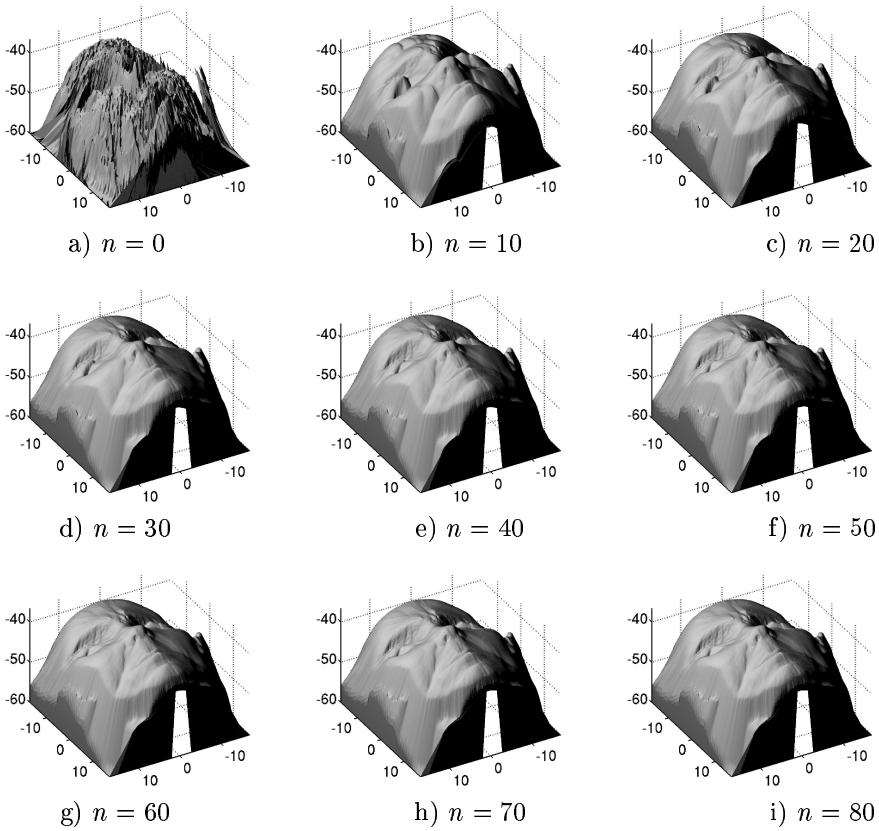

Figure 30: Evolution of the reconstructed surfaces in the course of the iterations (n=number of iterations).

A Some lemmas and their proofs

Lemma 1 *If J is differentiable on the smooth*[35] *and bounded set Ω and if for all x in Ω, $|\nabla J(x)|$ and $J(x)$ are upper bounded, then for all $p \in \mathbb{R}^2$, the function T_p (defined at the page 11) is Lipschitz continuous with a Lipschitz' constant of the form $\alpha(1+|p|)$ (α does not depend on p).*

Proof of Lemma 1. Let us denote R_p the function defined by

$$R_p : x \mapsto \sqrt{f^2|p|^2 + (x \cdot p)^2 + Q(x)^2}.$$

- Since Ω is bounded, one can verify that for all x in Ω,

$$R_p(x) \leq \alpha_2(1+|p|)$$

$$\text{and} \quad |\nabla R_p(x)| \leq \alpha_3(1+|p|).$$

- Also, we have for all x in Ω,

$$\begin{aligned} |\nabla T_p(x)| &\leq |\nabla J(x)|\ R_p(x) + |J(x)||\nabla R_p(x)| \\ &\leq \alpha(1+|p|). \end{aligned} \tag{37}$$

If Ω is convex, the conclusion follows by using the Mean value theorem.
Else, we have

$$\forall x, y \in \overline{\Omega}, \qquad |T_p(x) - T_p(y)| \leq |\nabla T_p|_\infty L(x,y),$$

where $L(x,y)$ is the Euclidean geodesic distance in Ω, i.e.

$$L(x,y) = \inf\left\{ \int_0^1 |\xi'(t)|\ dt \quad | \quad \xi(t) \in W^{1,\infty}([0,1], \bar{\Omega}) \quad s.t. \quad \xi(0) = x \text{ and } \xi(1) = y \right\}.$$

It is known, [34], that for any fixed $x \in \overline{\Omega}$, $y \mapsto L(x,y)$ is *Lipschitz continuous* in $\overline{\Omega}$ and that the Lipschitz constant does not depend upon x.

□

Lemma 3 *If the intensity image I verifies $\forall x \in \Omega,\ I(x) \geq \delta > 0$ then the solutions of (16) and (20) are bounded independently of φ.*

Proof of Lemma 3. Let us define $M = -\frac{1}{2} ln(\delta f^2)$.
We have:

$$H(x, M, 0) = -e^{-2M} + J(x)Q(x).$$

Since $Q(x) = \frac{I(x)f^2}{J(x)}$, we have

$$H(x, M, 0) = -e^{-2M} + I(x)f^2.$$

So by definition of M,

$$H(x, M, 0) \geq 0.$$

Therefore, the constant function M is a supersolution of (15) on Ω. Also, $\forall x \in \partial\Omega$ and $\forall \xi \in \mathbb{R}^2$, we have

$$H(x, M, \xi) = -e^{-2M} + J(x)\sqrt{f^2|\xi|^2 + (x \cdot \xi)^2 + Q(x)^2} \geq -e^{-2M} + J(x)Q(x) \geq 0.$$

So for all boundary conditions φ, the constant function M is a supersolution of (16) on $\overline{\Omega}$. It is also a supersolution of (20). Thus, by the strong uniqueness result (theorems 1 and 2), for all φ, the solution of (16) and (20) are upper bounded by M on Ω.

□

[35] i.e. if Ω is a locally Lipschitz continuous set.

References

[1] S.M. Bakshi. Shape from shading for non-lambertian surfaces. Master's thesis, University of Saskatchewan, July 1994.

[2] M. Bardi and I. Capuzzo-Dolcetta. *Optimal control and viscosity solutions of Hamilton-Jacobi-Bellman equations*. Birkhauser, 1997.

[3] G. Barles. *Solutions de Viscosité des Equations de Hamilton–Jacobi*. Springer–Verlag, 1994.

[4] G. Barles and P.E. Souganidis. Convergence of approximation schemes for fully nonlinear second order equations. *Asymptotic Analysis*, 4:271–283, 1991.

[5] Peter N. Belhumeur, David J. Kriegman, and Alan L. Yuille. The bas-relief ambiguity. *The International Journal of Computer Vision*, 35(1):33–44, November 1999.

[6] C. Brezinski. Convergence acceleration during the 20th century. *J. Comput. Appl. Math.*, 122:1–21, 2000.

[7] M.J. Brooks. Two results concerning ambiguity in shape from shading. In *AAAI-83*, pages 36–39, 1983.

[8] Alfred M. Bruckstein. On shape fron shading. *Computer. Vision Graphics Image Process*, 44:139–154, 1988.

[9] I. Capuzzo-Dolcetta and P.-L. Lions. Hamilton-jacobi equations with state constraints. *Trans. Amer. Math. Soc.*, 318(2):643–68, 1990.

[10] S.I. Cho and H. Saito. A Divide-and-Conquer Strategy in Shape from Shading problem. In *Proceedings of CVRP'97*, June 1997.

[11] F. Courteille, A. Crouzil, J.-D. Durou, and P. Gurdjos. Shape from Shading en conditions réalistes d'acquisition photographique. In *Proceedings of RFIA'04*, 2004.

[12] F. Courteille, A. Crouzil, J-D. Durou, and P. Gurdjos. Towards shape from shading under realistic photographic conditions. In *Proceedings of the International Conference on Pattern Recognition*, Cambridge, UK, August 2004. IAPR.

[13] M.G. Crandall, H. Ishii, and P.-L. Lions. User's guide to viscosity solutions of second order partial differential equations. *Bull. Amer. Soc.*, 27:1–67, 1992.

[14] M.G. Crandall and P.-L. Lions. Viscosity solutions of Hamilton–Jacobi equations. *Trans. AMS*, 277:1–43, 1983.

[15] A. Crouzil, X. Descombes, and J-D. Durou. A multiresolution approach for shape from shading coupling deterministic and stochastic optimization. *IEEE Transactions on Pattern Analysis and Machine Intelligence*, 25(11):1416–1421, November 2003.

[16] P. Dupuis and J. Oliensis. An optimal control formulation and related numerical methods for a problem in shape reconstruction. *The Annals of Applied Probability*, 4(2):287–346, 1994.

[17] J-D. Durou, M. Falcone, and M. Sagona. A survey of numerical methods for shape from shading. Research report 2004-2-R, IRIT, January 2004.

[18] J.-D. Durou and D. Piau. Ambiguous shape from shading with critical points. *Journal of Mathematical Imaging and Vision*, 12(2):99–108, 2000.

[19] M. Falcone and M. Sagona. An algorithm for the global solution of the shape-from-shading model. *International Conference on Image Analysis and Processing*, 1:596–603, 1997. LNCS 1310.

[20] M. Falcone, M. Sagona, and A. Seghini. A scheme for the shape-from-shading model with "black shadows". In *Proceedings of ENUMATH 2001*, 2001.

[21] D. Forsyth and A Zisserman. Reflections on shading. *IEEE Transactions on Pattern Analysis and Machine Intelligence*, 13(7):671–679, July 1991.

[22] J.K. Hasegawa and C.L. Tozzi. Shape from shading with perspective projection and camera calibration. *Computers and Graphics*, 20(3):351–364, May 1996.

[23] G. Hermosillo and O. Faugeras. Dense image matching with global and local statistical criteria: a variational approach. In *Proceedings of CVPR'01*, 2001.

[24] A. Heyden, G. Sparr, M. Nielsen, and P. Johansen, editors. Copenhagen, Denmark, May 2002. Springer–Verlag.

[25] B.K. Horn. *Robot Vision.* MIT Press, 1986.

[26] B.K. Horn and M.J. Brooks, editors. *Shape from Shading.* The MIT Press, 1989.

[27] B.K.P. Horn. Obtaining shape from shading information. In P.H. Winston, editor, *The Psychology of Computer Vision.* McGraw-Hill, New York, 1975.

[28] IEEE Computer Society. Nice, France, 2003. IEEE Computer Society Press.

[29] R. Kimmel and A.M. Bruckstein. "Global shape-from-shading". *CVGIP: Image Understanding*, pages 360–369, 1995.

[30] R. Kimmel and J.A. Sethian. Optimal algorithm for shape from shading and path planning. *Journal of Mathematical Imaging and Vision*, 14(2):237–244, May 2001.

[31] Ron Kimmel and Alfred M. Bruckstein. Tracking level sets by level sets : A method for solving the shape from shading problem. *Computer Vision and Image Understanding*, 62(2):47–58, July 1995.

[32] K.M. Lee and C.C.J. Kuo. Shape from shading with perspective projection. *CVGIP: Image Understanding*, 59(2):202–212, 1994.

[33] K.M. Lee and C.C.J. Kuo. Shape from shading with a generalized reflectance map model. *Computer Vision and Image Understanding*, 67(2):143–160, August 1997.

[34] P.-L. Lions. *Generalized Solutions of Hamilton–Jacobi Equations.* Number 69 in Research Notes in Mathematics. Pitman Advanced Publishing Program, 1982.

[35] P.-L. Lions, E. Rouy, and A. Tourin. Shape-from-shading, viscosity solutions and edges. *Numer. Math.*, 64:323–353, 1993.

[36] T. Okatani and K. Deguchi. Reconstructing Shape from Shading with a Point Light Source at the Projection Center: Shape Reconstruction from an Endoscope Image. In *Proceedings of ICPR'96*, pages 830–834, August 1996.

[37] T. Okatani and K. Deguchi. Shape reconstruction from an endoscope image by shape from shading technique for a point light source at the projection center. *Computer Vision and Image Understanding*, 66(2):119–131, May 1997.

[38] T. Okatani and K. Deguchi. On classification of singular points for global shape from shading. In *Proceedings of the 3rd Asian Conference on Computer Vision*, volume 1351, pages 48–55, Hong Kong, January 1998. springer-verlag.

[39] T. Okatani and K. Deguchi. On identification of singular points using photometric invariants for global shape from shading problem. In *Proceedings of the International Conference on Pattern Recognition*, volume 2, pages 1787–1790, Brisbane, Australia, August 1998. Computer Society Press.

[40] J. Oliensis. Shape from shading as a partially well–constrained problem. *CVGIP: Image Understanding*, 54(2):163–183, 1991.

[41] J. Oliensis and P. Dupuis. A global algorithm for shape from shading. In *Proceedings of ICCV'93*, pages 692–701, 1993.

[42] S. Osher. A level set formulation for the solution of the dirichlet problem for a hamilton-jacobi equations. *SIAM Journal on Mathematical Analysis*, 24(5):1145–1152, 1993.

[43] S. Osher and J. Sethian. Fronts propagating with curvature dependent speed: algorithms based on the Hamilton–Jacobi formulation. *Journal of Computational Physics*, 79:12–49, 1988.

[44] M.A. Penna. Local and semi-local shape from shading for a single perspective image of a smooth object. *Computer Vision, Graphics, and Image Processing*, 46(3):346–366, 1989.

[45] A. Pentland. Local shading analysis. *IEEE Transactions on Pattern Analysis and Machine Intelligence*, 6:170–187, 1984.

[46] E. Prados. PhD thesis, Université de Nice-Sophia Antipolis, 2004.

[47] E. Prados, F. Camilli, and O. Faugeras. A viscosity method for shape-from-shading without boundary data. Technical report, INRIA, 2004.

[48] E. Prados and O. Faugeras. A mathematical and algorithmic study of the lambertian SFS problem for orthographic and pinhole cameras. Technical Report RR-5005, INRIA, November 2003.

[49] E. Prados and O. Faugeras. "Perspective Shape from Shading" and viscosity solutions. In *Proceedings of the 9th International Conference on Computer Vision* [28], pages 826–831.

[50] E. Prados and O. Faugeras. A rigorous and realistic shape from shading method and some of its applications. Technical Report 5133, INRIA, March 2004.

[51] E. Prados and O. Faugeras. A rigorous lambertian shape-from-shading method for orthographic and pinhole cameras. *Submitted to IJCV*, 2004.

[52] E. Prados and O. Faugeras. Unifying approaches and removing unrealistic assumptions in Shape from Shading: Mathematics can help. In *Proceedings of ECCV'04*, 2004.

[53] E. Prados, O. Faugeras, and E. Rouy. Shape from shading and viscosity solutions. In Heyden et al. [24], pages 790–804.

[54] E. Prados, O. Faugeras, and E. Rouy. Shape from shading and viscosity solutions. Technical Report 4638, INRIA, November 2002.

[55] H. Ragheb and E.-R. Hancock. Highlight removal using shape-from-shading. In Heyden et al. [24], pages 626–641.

[56] E. Rouy and A. Tourin. A Viscosity Solutions Approach to Shape-from-Shading. *SIAM Journal of Numerical Analysis*, 29(3):867–884, June 1992.

[57] J.A. Sethian and J. Strain. Crystal growth and dendritic solidification. *Journal of Computational Physics*, 98:231–253, 1992.

[58] H. M. Soner. Optimal control with state space constraints. *SIAM J. Contr. Optim*, 24:Part I: 552–562, Part II: 1110–1122, 1986.

[59] A.J. Stewart and M.S. Langer. Toward accurate recovery of shape from shading under diffuse lighting. *IEEE Transactions on Pattern Analysis and Machine Intelligence*, 19(9):1020–1025, September 1997.

[60] P. Tan, S. Lin, L. Quan, and H.Y. Shum. Highlight removal by illumination-constrained inpainting. In *Proceedings of the 9th International Conference on Computer Vision* [28], pages 164–169.

[61] A. Tankus, N. Sochen, and Y. Yeshurun. A new perspective [on] Shape-from-Shading. In *Proceedings of the 9th International Conference on Computer Vision* [28], pages 862–869.

[62] Y.L Tian, H.T. Tsui, S.Y. Yeung, and S. Ma. Shape from shading for multiple light sources. *Journal of the Optical Society of America A*, 16(1):36–52, January 1999.

[63] T. Wada, H. Ukida, and T. Matsuyama. Shape from shading with interreflections under proximal light source-3D shape reconstruction of unfolded book surface from a scanner image. In *Proceedings of ICCV'95*, June 1995.

[64] I. Weiss. A perspective 3D formalism for shape from shading. In *Proceedings of DARPA Image Understanding Workshop*, volume 2, pages 1393–1402, May 1997.

[65] S.Y. Yuen, Y.Y. Tsui, Y.W. Leung, and R.M.M. Chen. Fast marching method for shape from shading under perspective projection. In *Proceedings of VIIP'02*, pages 584–589, September 2002.

[66] R. Zhang, P.-S. Tsai, J.-E. Cryer, and M. Shah. Shape from Shading: A survey. *IEEE Transactions on Pattern Analysis and Machine Intelligence*, 21(8):690–706, August 1999.

List of Figures

Contents

Unité de recherche INRIA Sophia Antipolis
2004, route des Lucioles - BP 93 - 06902 Sophia Antipolis Cedex (France)

Unité de recherche INRIA Futurs : Parc Club Orsay Université - ZAC des Vignes
4, rue Jacques Monod - 91893 ORSAY Cedex (France)
Unité de recherche INRIA Lorraine : LORIA, Technopôle de Nancy-Brabois - Campus scientifique
615, rue du Jardin Botanique - BP 101 - 54602 Villers-lès-Nancy Cedex (France)
Unité de recherche INRIA Rennes : IRISA, Campus universitaire de Beaulieu - 35042 Rennes Cedex (France)
Unité de recherche INRIA Rhône-Alpes : 655, avenue de l'Europe - 38334 Montbonnot Saint-Ismier (France)
Unité de recherche INRIA Rocquencourt : Domaine de Voluceau - Rocquencourt - BP 105 - 78153 Le Chesnay Cedex (France)

Éditeur
INRIA - Domaine de Voluceau - Rocquencourt, BP 105 - 78153 Le Chesnay Cedex (France)
http://www.inria.fr
ISSN 0249-6399